Physics of Plasmas

Hydroscaling indirect-drive implosions on the National Ignition Facility

Cite as: Phys. Plasmas **29**, 062705 (2022); https://doi.org/10.1063/5.0080732
Submitted: 02 December 2021 • Accepted: 01 May 2022 • Published Online: 02 June 2022

K. L. Baker, O. Jones, C. Weber, et al.

Physics of Plasmas ARTICLE scitation.org/journal/php

Hydroscaling indirect-drive implosions on the National Ignition Facility

Cite as: Phys. Plasmas **29**, 062705 (2022); doi: 10.1063/5.0080732
Submitted: 2 December 2021 · Accepted: 1 May 2022 ·
Published Online: 2 June 2022

K. L. Baker,[1,a)] O. Jones,[1] C. Weber,[1] D. Clark,[1] P. K. Patel,[1] C. A. Thomas,[2] O. L. Landen,[1] R. Nora,[1] G. J. Anderson,[1] J. Gaffney,[1] S. MacLaren,[1] D. T. Casey,[1] T. Döppner,[1] E. L. Dewald,[1] R. Tommasini,[1] B. K. Spears,[1] J. Salmonson,[1] M. Hohenberger,[1] S. Khan,[1] A. Zylstra,[1] A. Kritcher,[1] P. Amendt,[1] V. Smalyuk,[1] J. Lindl,[1] C. Young,[1] J. S. Ross,[1] D. Ho, O. A. Hurricane,[1] D. A. Callahan,[1] T. Woods,[1] J. L. Milovich,[1] D. J. Strozzi,[1] B. Bachmann,[1] R. Bionta,[1] P. M. Celliers,[1] D. Fittinghoff,[1] R. Hatarik,[1] M. Gatu Johnson,[3] K. Meaney,[4] M. Millot,[1] P. L. Volegov,[4] and C. Wilde[4]

AFFILIATIONS

[1]Lawrence Livermore National Laboratory, Livermore, California 94550, USA
[2]Laboratory for Laser Energetics, University of Rochester, Rochester, New York 14623, USA
[3]Massachusetts Institute of Technology, Cambridge, Massachusetts 02139, USA
[4]Los Alamos National Laboratory, Los Alamos, New Mexico 87544, USA

[a)]**Author to whom correspondence should be addressed:** baker7@llnl.gov

ABSTRACT

A goal of the laser-based National Ignition Facility (NIF) is to increase the liberated fusion energy "yield" in inertial confinement fusion experiments well past the ignition threshold and the input laser energy. One method of increasing the yield, hydrodynamic scaling of current experiments, does not rely on improving compression or implosion velocity, but rather increases the scale of the implosion to increase hot-spot areal density and confinement time. Indirect-drive (*Hohlraum* driven) implosions carried out at two target sizes, 12.5% apart, have validated hydroscaling expectations. Moreover, extending comparisons to the best-performing implosions at five different capsule sizes shows that their performance also agrees well with hydroscaling expectations even though not direct hydroscales of one another. In the future, by switching to a reduced loss *Hohlraum* geometry, simulations indicate that we can drive 20% larger-scale implosions within the current power and energy limitations on the NIF. At the demonstrated compression and velocity of these smaller-scale implosions, these 1.2× hydroscaled implosions should put us well past the ignition threshold.

I. INTRODUCTION

There are many approaches that attempt to improve the quality of current *Hohlraum*-driven capsule implosions. These include lowering the entropy (adiabat) of the imploding shell to enable higher compression[1] and increasing the peak velocity. Lowering the adiabat can encompass many areas such as the initial choice of the laser pulse shape, capsule dopant to protect the ice–ablator interface from higher, more penetrating x rays, optimizing shock timing and strength and reducing hydrodynamic instabilities such that implosions behave closer to their as-designed adiabat. Other approaches such as increasing the peak velocity and hence capsule fuel imploding kinetic energy at a fixed *Hohlraum* radiation drive temperature leads to more capsule ablator material ablated as described by the rocket equation. This increases the threat of feedthrough of hydrodynamic instabilities and decreases the final confining capsule areal density, so in practice there is a limit to the maximum velocity that these implosions can be driven. The capsule-absorbed energy can also be increased by using a smaller *Hohlraum* at fixed input laser power to increase the drive temperature and hence ablation pressure and scaling up the ablator and ice thickness, keeping the radius constant.[2] This approach increases the difficulty of controlling implosion symmetry. Hydrodynamic scaling, which is the subject of this study, is perhaps the lowest physics risk to increasing the performance of implosions. Hydroscaling is accomplished by increasing the scale and hence the mass of the implosion, not by trying to improve the quality or compression of the implosion or by increasing the implosion velocity.

Hydroscaling uses hydroequivalent implosions, which are designed to achieve the same no-alpha heating stagnation pressure,

implosion velocity, shell adiabat, and scaled radiation temperature inside the *Hohlraum* in indirect-drive inertial confinement fusion.[3] Since the hydrodynamic Euler equations are invariant to the transformation $x' \Rightarrow Sx$ and $t' \Rightarrow St$,[3,4] hydroscaled implosions lead to the same hydrodynamic behavior if the implosion velocities $\sim x/t$ and x'/t' are kept the same. The implosion velocity can be kept the same by modifying the laser drive pulse to keep the temporally scaled radiation temperature inside the *Hohlraum* the same between implosions. Figure 1 shows a schematic of the hydroscaling approach, where all spatial dimensions, x, and time, t, are increased by the scale factor S, and the laser power, P_L, is nominally increased by S^2 and hence the laser energy, E_L, by S^3. If both the surface area of the *Hohlraum*, A_h, and the laser power are increased by S^2, then the scaled radiation temperature in the *Hohlraum* $[P_L \times S^2/(\sigma A_h S^2)]^{0.25}$ is independent of scale, ignoring for the moment the fact that the losses from diffusive Marshak wave propagation into the *Hohlraum* wall drop in time. By maintaining the same scaled radiation temperature in the *Hohlraum* and modifying the capsule to maintain the same dopant optical depth and implosion velocity, the shell adiabat and no-alpha heating pressure can be maintained between hydroscaled implosions.

In Sec. II of this study, we look at the limitations of performing a direct hydroscaling on the National Ignition Facility (NIF). This section discusses both physics limitations and practical limitations. In Sec. III, we discuss two approaches to hydroscaling the capsule in the experiments to preserve the velocity, opacity, and density profiles between the hydroscaled implosions. In Sec. IV, we present the four direct hydroscaling experiments that were performed for this study. These experiments hydroscaled the entire target, both the *Hohlraum* and the capsule. In Sec. V, we present additional results from two subscale and seven full-scale BigFoot experiments that were not strictly hydroscaled implosions. These implosions bolster the results from Sec. IV and provide further scale dependencies of other hotspot parameters. In Sec. VI, we compare the best-performing implosions spanning several drive designs and five high-density carbon (HDC) capsule scales, ranging from an inner radius of 0.844–1.05 mm. In Sec. VII, we discuss ways in which hydroscaling to larger capsules can be performed on the National Ignition Facility within the current energy and power limitations by reducing the losses of the *Hohlraum* to go well beyond the ignition threshold. In Sec. VIII, we summarize our results that were presented in this study.

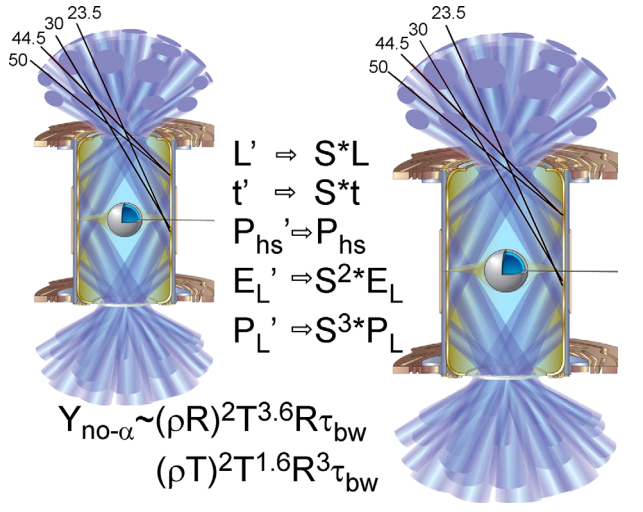

FIG. 1. Ideal Euler scaling with schematic of typical *Hohlraum* scale change of 12%.

II. LIMITATIONS ON STRAIGHT HYDROSCALING

There are several practical and physics-based limitations that prevent a straight hydroscaling of all parameters from being performed in indirect-drive inertial confinement fusion (ICF). One of the practical limitations of performing this study on the NIF is the phase plates on each of the quads of the laser. For a strict hydroscaling, the size of the elements comprising the phase plates themselves would have to be scaled to maintain the same intensity on the *Hohlraum* wall, which from a cost perspective is impractical. Because the phase plates are not scaled, the per beam intensity on the *Hohlraum* wall is higher for the larger-scale *Hohlraums* due to the increase in power $\sim S^2$ for a straight scale. This higher intensity on the wall then has several potential effects, which interfere with the straight scaling. The higher intensity can cause changes to the spectrum of radiation driving the capsule, and the higher intensities, I, can result in higher levels of laser-plasma instabilities, LPI. An increased level of LPI scatters more energy out of the *Hohlraum* from stimulated Raman and Brillouin scattering, which leads to higher hot-electron preheat of the fuel for stimulated Raman scattering and two plasmon decay and might lead to higher levels of cross-beam energy transfer, $\sim I$, which can affect the shape of the implosion. The higher intensity for the larger-scale *Hohlraums* also increases the plasma temperature, where the beams interact with the *Hohlraum* wall plasma. This higher temperature causes a higher expansion velocity of the gold bubble from the wall, which moves the outer laser spots closer to the *Hohlraum* axis,[5] driving the capsule harder on the pole. To maintain drive symmetry, the inner beam cone fraction for the larger-scale *Hohlraums* is increased from 31% to 34% for the two scales presented below.

In two-dimensional simulations, the laser energy is symmetrized in azimuth along the *Hohlraum* wall, which lowers the beam intensity in the simulations relative to the experiments where the laser energy is focused at discreet locations along the azimuth, at least until the wall moves in and the individual quads can begin to fill in the azimuth. As such, one would expect a P2 shape offset between experiments and simulations due to a difference in laser intensity, which should make the experiments more oblate that the two-dimensional simulations predict. This offset between experiments and simulations would be *Hohlraum* diameter-dependent, and when hydroscaling the entire target, the initial intensity in the experiments scales as S^2 and in the simulations as S since the beam area in the simulations increases as S but stays approximately constant in the experiments. This implies that the offset in shape between the two-dimensional simulations and experiments would change with scale.

Additional deviations from straight scaling include engineering features. Figure 2 shows an exploded view of the *Hohlraum* targets with each of the components. Some of these features were kept constant between the scales, including the glue attaching the fill tube to the capsule, the thickness of the tent (45 nm formvar, $C_{31}H_{56}O_{13}$ at 1.23 g/cm^3) holding the capsule in the *Hohlraum*, the laser entrance hole (LEH) window (500 nm polyimide, $C_{22}H_{10}N_2O_5$ at 1.43 g/cm^3) that holds in the low-density *Hohlraum* ^{4}He fill gas at cryogenic

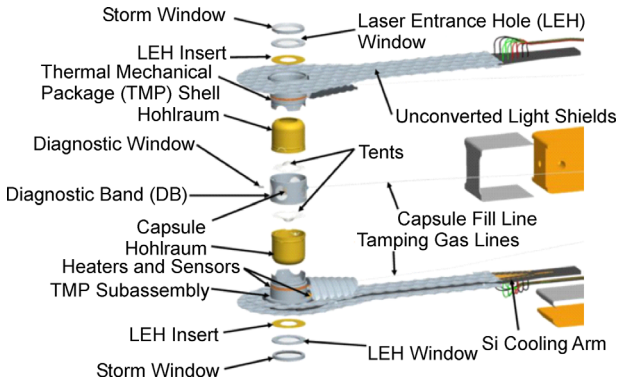

FIG. 2. Exploded view diagram of an indirect-drive target used for layered implosions.

temperatures, and the storm window (100 nm polyimide) that protects from ice condensation on the polyimide foil. Exact dimensions of the *Hohlraum* (radius, length, and LEH radius), pointing differences and exact capsule dimensions and dopant concentrations in the capsules slightly varied from exact scales, <1%. As we will discuss later, the fill tubes used in the experiments either stayed the same as the scale was changed or in some initial experiments were larger in the smaller-scale experiments. The fill tube diameter, according to simulations, affects the amount of material injected into the hotspot through hydrodynamic instabilities, which could have an outsized effect on the smaller hotspot associated with the smaller-scale implosions.

A straight scaling of the laser pulse would also lead to physics changes between the scales and break drive symmetry equivalence. For instance, the same energy at the front of the laser pulse (picket) is used to burn through the unscaled thin polyimide foil and the storm window such that a smaller percentage of energy would reach the wall. This affects the inner beams more than the outer beams as they are primarily used to burn through the windows and due to their longer burn through distance in the *Hohlraum* gas. In the direct hydroscaling experiments described in Sec. IV, this was partially compensated for by increasing the energy in the foot by ~5% in the smaller-scale experiments.

Physics-based limitations for hydroscaling include the diffusive (hence nonlinear in time) Marshak wave penetration time into the wall, fixed capsule opacity and thermal conduction lengths, and exponentiating alpha heating. For the larger-scale *Hohlraums*, the length of the laser pulse (and implosion time) is increased by the scale factor, S. The diffusive Marshak wave, therefore, has a longer time to slow down as it penetrates into the *Hohlraum* wall, which results in a higher wall albedo than present in the smaller-scale *Hohlraum* with a straight scale. As such to maintain a given radiation temperature in the *Hohlraum*, less laser power is required than the straight scale of S^2 would predict. At the same time, however, more of the laser energy is scattered out of the *Hohlraum* due to LPI, as mentioned above for the larger-scale *Hohlraums* because the phase plates are not scaled. As discussed below, to account for this, the power was scaled as $S^{1.6}$ vs the straight S^2 scaling. A larger-scale capsule also leads to a longer hotspot temperature gradient, reducing thermal conduction losses, and to a higher hotspot areal density, increasing the fraction of the alpha particles redepositing their energy. Both effects lead to higher hotspot temperatures. The former leads to an additional yield contribution scaling as $S^{0.4}$.[3]

Another physics limitation is how the ablation front and fuel–ablator growth factors scale when two implosions are hydroscaled. Two-dimensional radiation hydrodynamic simulations indicate that the ablation front growth factors, $\sim\exp^{\gamma t}$, increase with scale due to the fixed ablation front scale length L, as shown for four different scales in Fig. 3(a) vs mode number ℓ. This can be understood from the following widely used analytic approximation for the ablation front RT growth factors for a capsule of initial radius R subject to a fixed ablation rate v_a and resultant fixed in time acceleration g:[6,7]

$$\gamma t \sim \sqrt{[(g\ell t^2/R)/(1+\ell L/R)]} - v_a \ell t/R$$
$$\sim \sqrt{[\ell/(1+\ell L/S)]} - v_a \ell,$$

where the final expression uses the hydroequivalences R and $t \sim S$ and $g \sim R/t^2 \sim 1/S$. In particular, the scale length term breaks the hydroequivalence as ℓ gets larger, reducing the ablation front scale length stabilization term $(1 + \ell L/S)$ as S increases as seen in Fig. 3. This leads to the peak ablation front growth factors increasing like $S^{3/4}$, as shown in Fig. 3(b), and the peak gradually shifting to a higher mode number as $S^{1/3}$.

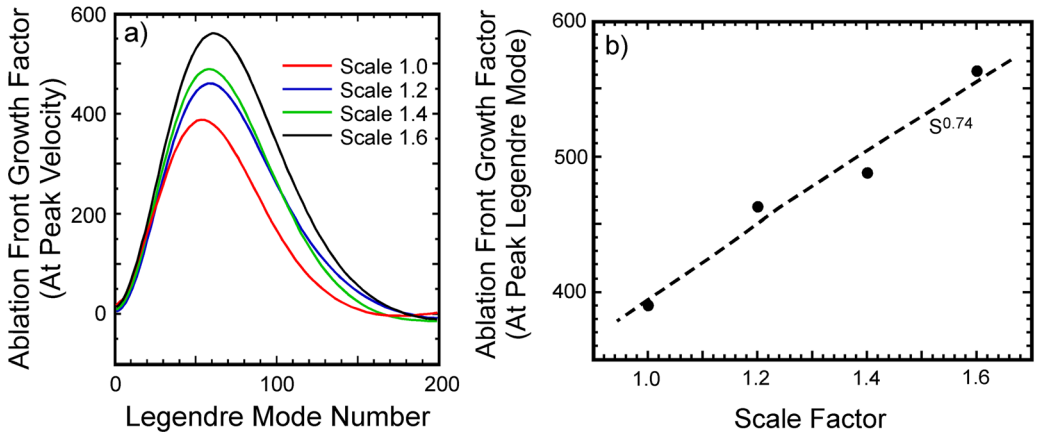

FIG. 3. (a) Ablation front growth factors at peak implosion velocity as a function of Legendre modes at different scales. (b) Peak ablation front growth factor, G_{fp}, at each scale fit with a power law to get the scaling, $G_{fp} \propto S^{0.74}$.

Another potential source of hydrodynamic instability growth is at the DT ice–ablator interface for which the growth factor classically scales as $\gamma t \sim \sqrt{(Ag\ell t^2/R)}$ and hence as $\sqrt{(A\ell)}$, where A is the Atwood number[7] describing the normalized density difference between the DT ice and nearby ablator (assumed positive for growth).

The capsule thickness and dopant concentration can be adjusted to keep the same Atwood number when hydroscaling and, therefore, keep the ice–ablator growth factors scale invariant in the simulations. The ablation front growth factors are also strong functions of the level of dopant concentration in the capsules through changing both L and v_a once the ablation front has reached the doped layer by peak power. For example, the current manufacturing capabilities led to ∼12.5% higher and ∼16% lower requested vs delivered dopant concentration as discussed in Secs. IV and V, respectively. A 14% increase in dopant percentage can increase the peak ablation front growth factors by ∼18%. We note that recent work on direct-drive cylindrical implosion experiments has reported that deceleration-phase Rayleigh–Taylor instability growth in those experiments could be kept scale invariant, maintaining the same growth factors to within ±15% with a factor of three difference in spatial scales.[8]

III. HYDROSCALING THE CAPSULE

A. Scaling Capsule Thickness $\propto S^{0.7}$ and Dopant $\propto S^{-1}$

In a strict hydroscale, all of the dimensions of the capsule would be scaled by S. However, two-dimensional radiation hydrodynamic simulations[9] suggest that maintaining the same density profile and velocity when hydroscaling a capsule to a smaller scale can be accomplished using an ablator thickness slightly thicker than a straight scale and increasing the dopant level as 1/S. The dopant adjustment is necessary to conserve the fixed ablator optical depth to hard x rays. The hard x-ray preheat distribution that is set by this optical depth is also an important factor in controlling the density distribution of the shell in flight and hence needs to be conserved to maintain similar hydrodynamic stability in the implosion. The thickness scaling is necessary to conserve the shell implosion velocity after the dopant concentration has been appropriately adjusted. This is the approach taken in Sec. IV. Figure 4(a) shows the results from a capsule-only simulation with the density and temperature profiles as a function of scaled radius for three different scale implosions. In particular, as the scale is increased from 1 to 1.2, the capsule thickness is decreased by 5 μm less than a straight scale, removed from the outermost undoped layer. This has the effect that the outer layer thickness sublinearly increases as $\sim S^{0.7}$ and that the total mass of the HDC ablator increases slower than S^3, as $\sim S^{2.6}$. Figure 4(b) shows that the implosion velocity as a function of scaled time can be made to match using this prescription. These simulations suggest that if this capsule scaling prescription is followed the two implosions share the same velocity and density profile inside the capsule. In the case of a smaller-scale capsule, which was 67 μm thick and had a dopant layer concentration of 0.32%, a 1.125 scale factor would then imply that a larger-scale capsule would be 72 μm thick ($67 \times 1.125^{0.7}$) and have a W dopant layer concentration of 0.28% (0.32/1.125).

B. Scaling Capsule Thickness $\propto S$ and Dopant $\propto S^{-2}$

Two-dimensional radiation hydrodynamic simulations also indicate that if all the dimensions in the capsule are scaled by S and the opacities of the entire capsule scaled by S^{-1} that the mass remaining

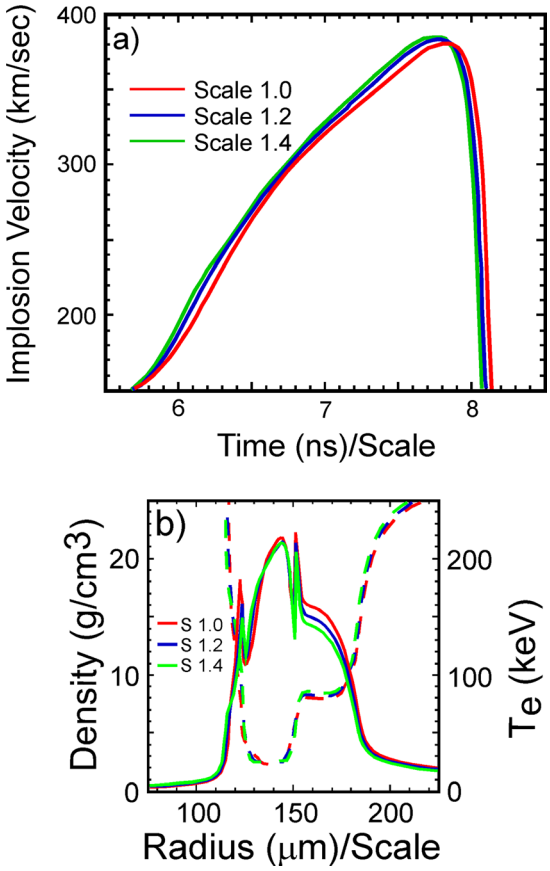

FIG. 4. (a) Velocity vs scaled time for three different scales. (b) Density and temperature profiles as a function of scaled radius near the time of peak implosion velocity for three different scales. The thickness of the capsule is scaled as $S^{0.74}$ and the dopant scaled as S^{-1}.

and fuel velocity are preserved, the latter is shown in Fig. 5(a). In addition, unlike the scaling in Sec. III A, the ablation front scale length also scales, as shown in Fig. 5(b), which preserves the ablation front growth factors as the capsule is hydroscaled. The opacity of the undoped HDC material, however, cannot be reduced by S^{-1} in experiments, but the doped layer can be decreased by more than S^{-1} such that the entire opacity of the ablator is reduced by $\sim S^{-1}$. This approach was taken in Sec. V. All the capsule dimensions were scaled by S, but in order to recover the Atwood number and approximate a reduction in the entire capsule of 1/S, the dopant concentration was more strongly decreased, approximately as S^{-2}. For example, a smaller capsule 64 μm thick with a 0.35% W dopant layer hydroscaled by a factor of S = 1.125 leads to a $64 \times 1.125 = 72$-μm-thick capsule containing a $0.35/1.125^2 = 0.28\%$ W dopant layer. Figure 5(c) compares two-dimensional simulations of the density profile as a function of scaled radius for the larger scale, N180128, vs subscale implosion with the dopant increased by S and S^2. There is very good agreement in the density profiles at the three times between the larger-scale implosion and the directly scaled smaller implosion with the dopant increased by S^2.

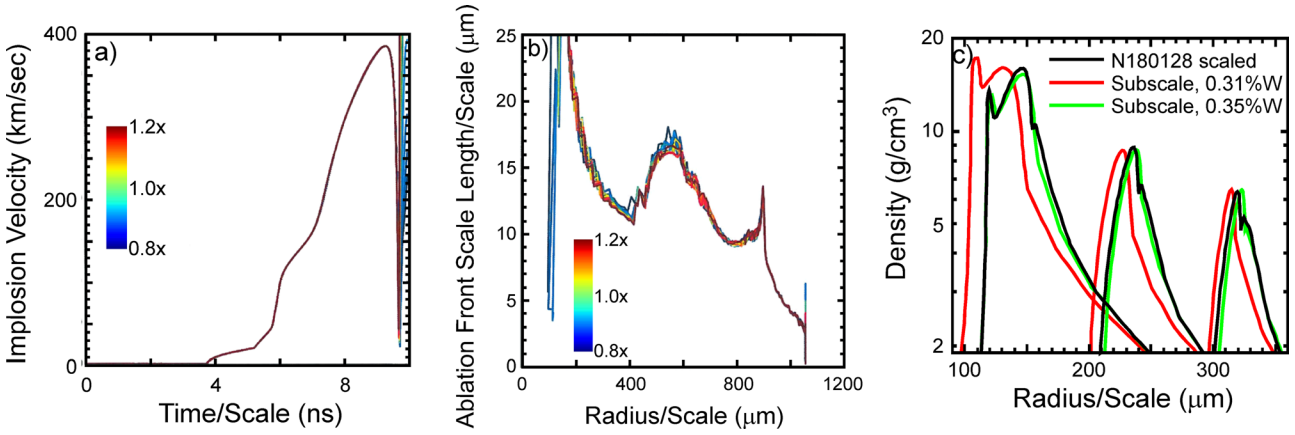

FIG. 5. (a) Velocity vs scaled time as a function of scale with the opacity of the entire capsule proportional to S^{-1}.(b) Ablation front scale lengths divided by scale vs scaled radius with the opacity of the entire capsule proportional to S^{-1}. (c) Density as a function of scaled radius for three different times during an implosion. The thickness of the capsule is scaled like S and the dopant as scaled as S^{-2} for the solid green line (simulating the opacity of the entire capsule proportional to S^{-1}). The solid black lines represent the implosion of the large-scale capsule with the radius reduced by the scale factor. The solid red lines represent Euler-scaled implosions, $L' = SL$, with the dopant scaled as S^{-1}. The solid green lines represent Euler-scaled implosions, $L' = SL$, with the dopant scaled as S^{-2}.

IV. DIRECT HYDROSCALING EXPERIMENTS: CAPSULE THICKNESS α $S^{0.7}$

A direct hydroscaling campaign was conducted on the National Ignition Facility based on the shot yielding the highest inferred yield amplification (alpha heating contribution) on the NIF at the time, N180128. This campaign hydroscaled the entire system downward, both the capsule and the *Hohlraum* by a scale factor of 1/1.125.[10,11] Scaling the entire system to a larger dimension, both capsule and *Hohlraum*, was not possible in cylindrical *Hohlraums* due to limitations in laser power and energy. A split schematic of the two target scales is displayed in Fig. 6, which shows the smaller scale on top and the larger scale on the bottom. The BigFoot platform was used for these experiments, whose salient characteristics are described in Appendix A.[2,10,12–15]

A. Experimental Parameters and 1D Results

The capsules used in the larger-scale shots, had an inner radius of 950 μm, were 72.3 μm thick with an inner clean layer of 6.3 μm, a W-doped HDC layer that was 21.4 μm, and a clean outer layer that was 44.5 μm thick. The smaller-scale capsules, had an inner radius of 844 μm, an ablator wall thickness of 68.3 μm with an inner clean layer of 6 μm, a W-doped HDC layer that was 21.9 μm, and a clean outer layer that was 40.4 μm thick. This capsule scaling was intended to follow the prescription detailed in Sec. III A. The as-delivered smaller-scale capsules were thicker than requested, 68.3 vs 66.7 μm, and had less dopant than requested, a dopant ρR of 5.26 vs 6.0 μm%. The reduced dopant in the smaller-scale capsules reduced the ablation front growth factors in those implosions by a larger degree than the $S^{0.7}$ scaling indicated above for the idealized scaling as shown in Fig. 7, which shows two-dimensional growth factors from a set of capsule-only simulations. The ice layer formed on the inside surface of the HDC shell was hydrodynamically scaled along with the capsules with the larger capsules containing a 49.6-μm-thick ice layer and the smaller-scale capsules containing a 44.5-μm-thick ice layer.

The pulse shapes for the two scales are shown in Fig. 8. The pulse shape for the larger scale *Hohlraum*, N180128, is shown as the solid black line and for the smaller scale, N190617, as the solid red line. Two scaled versions of the larger scale pulse are also shown. Both are scaled in time, $t' = t/S$. The dashed black line is scaled in power by $S^{1.44}$ and the solid blue line by S^2. The scaling by S^2 represents a straight Euler scaling. To maintain the same temperature while accounting for the lower wall albedo reached in the shorter pulse, smaller-scale *Hohlraum* necessitates weaker power scaling $\sim S^{1.6}$. In addition, because the smaller-scale capsules were delivered thicker

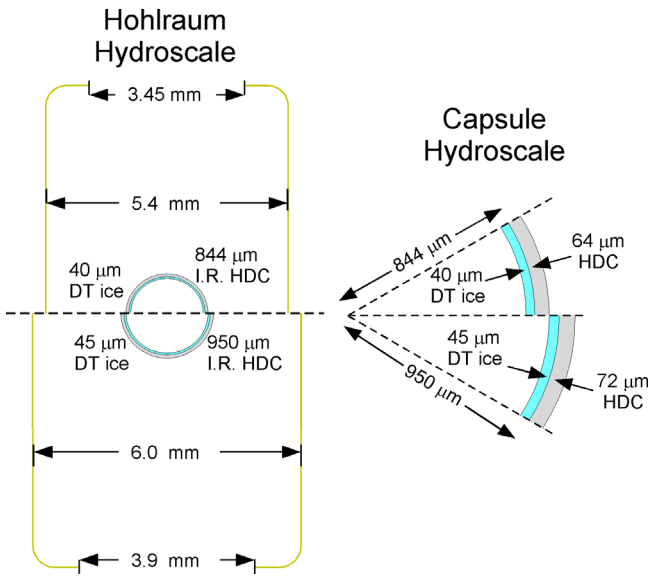

FIG. 6. Hydroscaled target comparison between a 5.4-mm *Hohlraum* and an 844-μm inner radius capsule (top) vs a 6.0-mm *Hohlraum* and a 950-μm inner radius capsule (bottom).

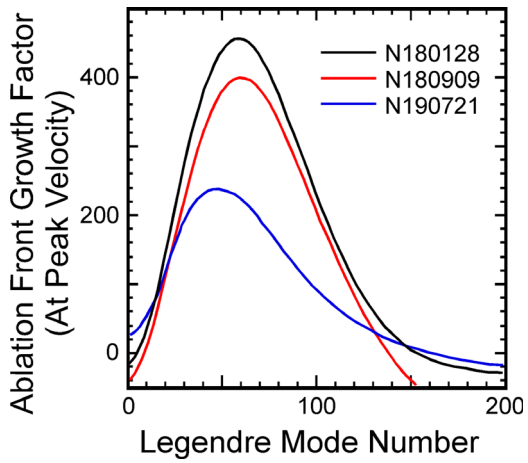

FIG. 7. The ablation front growth factors at peak implosion velocity as a function of Legendre modes for the two scales used in the direct hydroscaling experiments. The variation between repeat shots at the same scale can be seen between the black (N180128) and red (N180909) lines. The smaller-scale ablation front growth factors, blue, are significantly reduced due to the lower dopant in the as-delivered subscale capsules.

than requested, an even slower power scaling was used, $S^{1.44}$, to maintain the implosion velocity.

The radiation temperature profiles for the two scales were measured using the DANTE x-ray power diagnostic.[16] Unfortunately, during the time period that the two larger-scale implosions, N180128 and N180909, were conducted, there was an issue with the diagnostic's clipper circuit, which saturated the signals when channel voltages were too high, near peak power. DANTE was available when the same laser pulse shape was used in a gold-lined uranium *Hohlraum*, N190730. It is expected that the gold-lined uranium *Hohlraum* increases the peak radiation temperature inside the *Hohlraum* by as much as 1.8% over that of a gold *Hohlraum* due to the increased wall albedo.[17] Figure 9

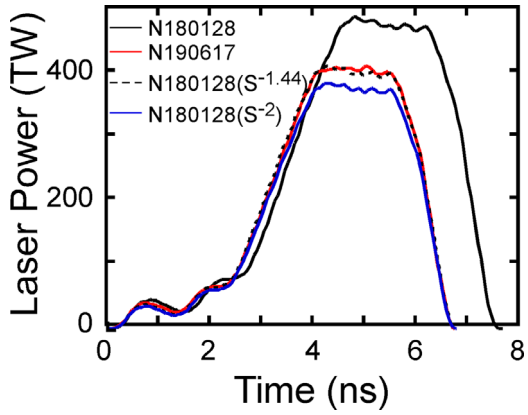

FIG. 8. Laser power as a function of time for the larger scale N180128 implosion (solid black line) smaller-scale N190617 implosion (solid red line), Euler-scaled N180128 with power $\sim S^2$ and time $\sim S$ (solid blue line), and accounting for *Hohlraum* albedo and thicker capsule, power $\sim S^{1.44}$ and time $\sim S$ (dashed black line).

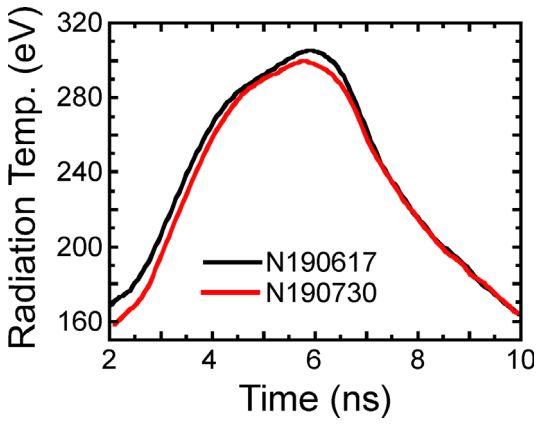

FIG. 9. *Hohlraum* radiation temperature profiles as unfolded from the DANTE diagnostic for U-lined Au *Hohlraum* N190730 (solid red line) and smaller-scale Au *Hohlraum* N190617 (black line).

shows the radiation temperature profile from the full-scale gold-lined uranium *Hohlraum*, N190730, as the solid red line and from the subscale gold *Hohlraum* as the solid black line, N190617. The timescale for the larger scale shot, N190730, has been Euler scaled, $t' = t/1.125$, to better compare the two temperature profiles. The radiation temperature for the smaller-scale experiment, N190617, is at a slightly higher temperature than the full-scale experiment, N190730, because the power was increased to account for the slightly thicker than requested capsule so as to maintain the implosion velocity. This shot was expected to have a higher fluence by ~7% at peak power than the gold *Hohlraum*.

Figure 10 shows ten measured 1D hotspot parameters for the four hydroscaling implosions plotted as a function of the capsule scale. All data scaling is in agreement with the listed analytic scaling[18] within error bars. The reasons for the bifurcation between pairs of shots in yield, yield amplification, and other hotspot parameters are due to low-mode perturbations as discussed in Sec. IV B.

B. 2D Results: Corrections for Low-Mode Perturbations

The implosions are degraded by numerous low-mode perturbations. The low-mode perturbations are caused by the inner beam cone fraction used, cross-beam energy transfer (CBET) between cones near the LEH, the laser delivery and drift over time, capsule thickness variations, time-dependent *Hohlraum* wall motion, *Hohlraum* perturbations, and *Hohlraum* misalignment. The two largest low-order degradation mechanisms are due to m1/P1[19–21] and P2[10,13] Legendre modes. The P1/m1 degradations can be expressed as the difference in the max and min of areal density divided by the average areal density.[19] Figure 11 shows the areal density sky measured by fNADs[22,23] for each of the four implosions used in the direct hydroscaling campaign, which can be used to infer degradations from $m = 1$ low-mode asymmetries. The primary neutron images show the P2 degradation from the four implosions as displayed in Fig. 12.

The fNAD data and the hotspot shape both indicate that the pairs of shots N180128 and N190721 have similar low-mode perturbations as do the pair of shots N180909 and N190617. The first full-scale pair and subscale pair, N180128 and N190721, have virtually the

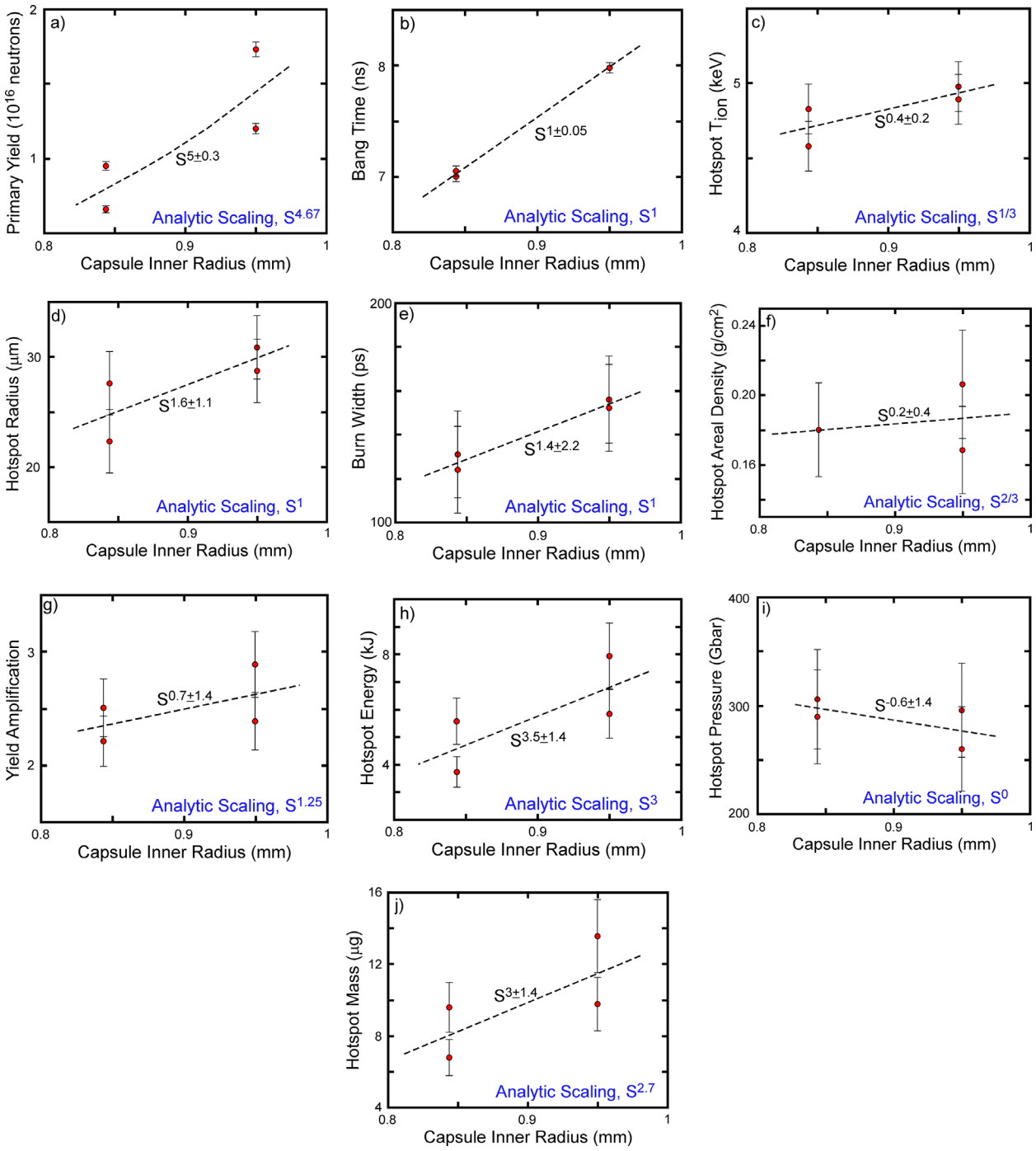

FIG. 10. Hotspot parameter scaling for the direct-drive implosions with capsule size/scale, S. A primary neutron yield, b) bang time, c) ion temperature, d) hotspot radius, e) burn width increasing, f) hotspot areal density, g) yield amplification, h) hotspot energy, i) hotspot pressure, and j) hotspot mass.

same, extremely small, degradation from shape, P2, and from P1/M1. In the case of the second pair, the subscale shot N190617 has a larger P2/P0 but smaller M1/P1 than the full-scale shot, N180909, so the degradation mechanisms are expected to counterbalance one another. We thus feel justified to take the ratio of the total yields for each pair separately yielding $1.95 \times 10^{16}/1.07 \times 10^{16} = 1.82$ and $1.35 \times 10^{16}/7.45 \times 10^{15} = 1.81$, the same number within the 3% error bars. These numbers would imply a yield scaling of $Y \propto S^{5.05}$ for a scale factor, S, of

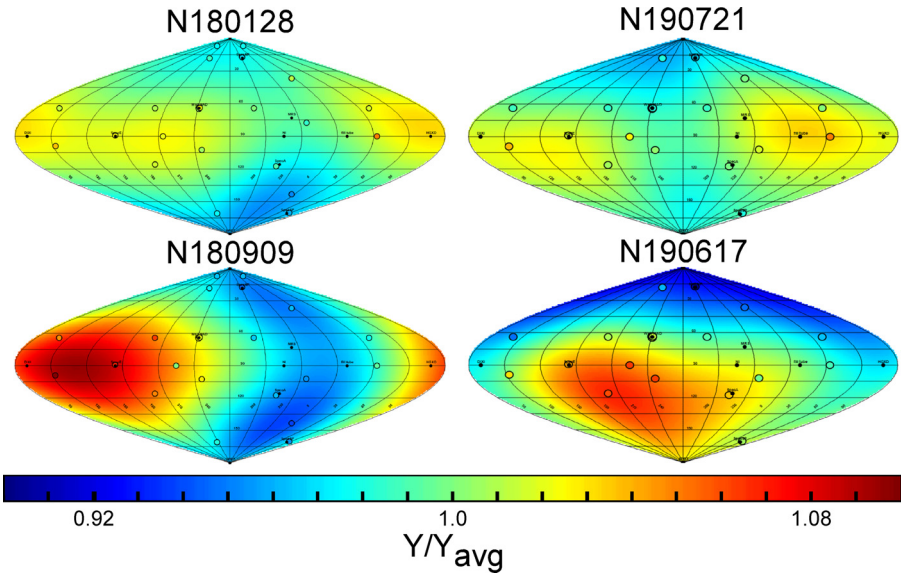

FIG. 11. Inferred areal density sky at bang time for the four implosions used in the direct hydroscaling campaign.

1.125. In estimating the scale dependence, however, we must remove the velocity dependence from the yields since the yield dependence on velocity is so high, $\sim v^{10}$.[10]

C. Velocity-Corrected Yield Scaling

The hydroscaling campaign had planned to do two one-dimensional convergent ablator experiments (1D-ConA) with a tritium-hydrogen-deuterium THD ice layer to directly measure the implosion velocity of the subscale and full-scale implosions.[24] We completed the subscale 1D-ConA experiment that provides a benchmark for the subscale simulations, which can then be used to estimate the relative velocities of the experimental pairs. In addition, as we will discuss in Appendix B, the experimental hotspot parameters inferred from all of the layered implosions in the overall BigFoot campaign can be used to estimate the relative velocities for the pairs of shots as well. The subscale 1D-ConA experiment used a laser-irradited iron foil placed, 12 mm from the imploding capsule, as an x-ray area backlighter A slit was then used to image the backlighter onto an x-ray streak camera with the imploding ablator's absorption providing the contrast. The geometry of the experiment is shown in Fig. 13(a). Figure 13(b) shows the raw radiography data, and Fig. 13(c) represents the inferred experimental radius as a function of time (red circles) from the radiograph along with a fit to the radius as a function of time using a rocket model[24–27] of the implosion along with the velocity as a function of time using the same model. The inferred peak ablator velocity in the experiment was 384 ± 10 km/s.

The ablator velocity in the 1D-ConA experiment is used to estimate the velocity of the ice layer in a DT implosion. According to simulations, the DT ice layer would be traveling at an ~6% higher velocity than the ablator material due to convergence effects, continuity equation, which would imply a peak implosion velocity (ice layer) in the 1D-ConA of ~407 ± 10 km/s. The 1D-ConA operated at a reduced energy relative to the DT-layered implosions due to large uncoated windows in the *Hohlraum* for the 1D-ConA and two missing quads used to backlight the capsule. The implosion velocity, v_{imp}, is related to the radiation temperature, T_r, by $v_{imp} \propto T_r^3$.[26] The radiation temperature, T_r, is also related to the laser energy, E_l, by $E_l \propto T_r^{3.5}$ such that $v_{imp} \propto E_l^{6/7}$.[16] When the reduced energy in the 1D-ConA relative to the layered implosions (laser delivery and the loss of two backlighter quads), ~70 kJ, and the lossy uncoated 1D-ConA windows (0.65 mm^2), ~10.5 kJ, are accounted for, and the peak velocity for the layered DT implosion, assuming $v_{imp} \propto E^{0.65}$, would be $407(1.35/1.27)^{6/7}$–428 km/s. Rocket model estimates of the peak implosion velocities for the four-layered implosions, N180128, N180909, N190617, and N190721, were determined to be 423, 424, 421, and 419 km/s, respectively. The rocket model estimates of N190617 and N190721 closely match the inferred DT-layered velocity from the 1D-ConA experiment of 428 km/s. Using the rocket model velocity estimates, the ratio of the total yields for the first full-scale and subscale pair, N180128 and N190721, is $1.95 \times 10^{16}(419/423)^{10}/1.07 \times 10^{16} = 1.7$. The ratio of the total yields for the second full-scale and

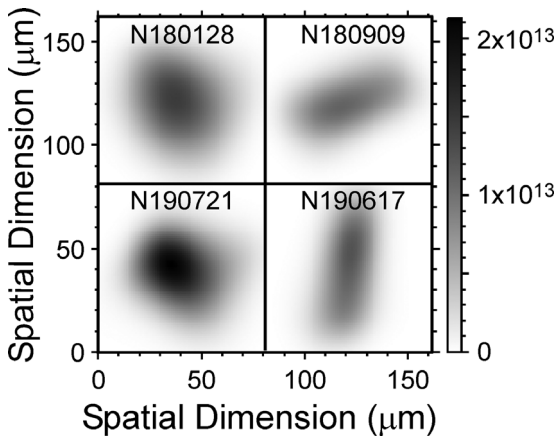

FIG. 12. Primary neutron images for the four implosions used in the direct hydroscaling campaign.

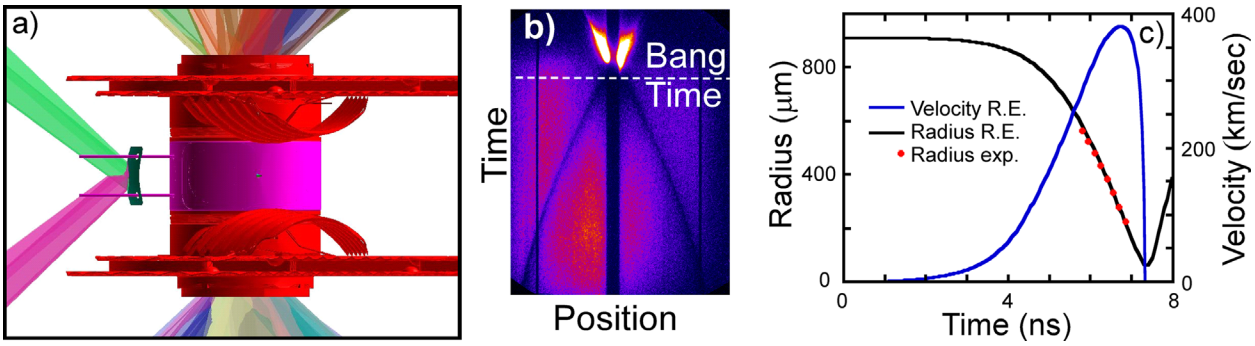

FIG. 13. (a) Schematic of the platform and the lasers impinging on the backlighter foil on the left and into the *Hohlraum* to drive the implosion on the right. (b) Raw radiography data from the iron backlighter radiographing the imploding ablator captured with an x-ray streak camera. (c) Inferred experimental radius as a function of time, red circles, fits using a rocket model with the simulated velocity (solid blue line) and the simulated radius as a function of time (solid black line).

subscale pair, N180909 and N190617, is $1.35 \times 10^{16}(421/424)^{10}/7.45 \times 10^{15} = 1.7$. Averaging these two results together implies an average yield ratio of 1.67 or a yield dependence $\propto S^{4.4}$, consistent with analytic scaling of $S^{4.4}$–$S^{4.7}$. The relative velocities of the four implosions, and hence the corrected yield dependence on scale, can also be estimated using the data from the entire BigFoot campaign as detailed in Appendix B.

V. COMPARISON OF SUBSCALE AND FULL-SCALE BIGFOOT SHOTS WITH VARYING IMPLOSION VELOCITIES: CAPSULE THICKNESS $\propto$ S

Over the course of the development of the BigFoot platform, described in Appendix A, two different *Hohlraum* sizes were utilized, which were approximately hydrodynamic scales of one another as shown in Fig. 6. The initial set of layered implosions was carried out at a design adiabat of four, $\alpha \sim 4$. In all cases, the capsules in these experiments were HDC ablators doped with tungsten (W) to shield the ice–ablator interface from x-ray preheat. The two lowest velocity implosions were carried out in a gold *Hohlraum*, 5.4 mm in diameter by 10.13 mm long, with an HDC capsule, which had an average 844-μm inner radius and 64.5-μm-thick HDC layer, containing 0.24% W dopant layer. The next few layered implosions were carried out in a hydrodynamically scaled gold *Hohlraum* with a scale factor of 1.125, 6 mm in diameter by 11.3 mm long, and capsules with an average 950-μm inner radius and a 72.3-μm-thick HDC layer. The exact capsule parameters are listed in Table I, where all the dimensions in the capsule are nominally scaled by S, but the dopant concentration remained unscaled on average instead of by S^{-2}. The two smaller-scale capsules used 10-μm-diameter fill tubes and the larger-scale implosions used 5-μm-diameter fill tubes. Recent symcap experiments using 10-μm fill tubes have estimated the injected mass at ~90 ng, which should reduce the yield of the smaller capsules relative to the larger capsules.[28] The pulse shape was also not a perfect hydrodynamic scale between the two sizes, which resulted in small differences in the implosion velocities for the larger-scale *Hohlraums* and the smaller-scale *Hohlraums* (Table II).

A. Experimental Results

The yield from the first five-layered implosions in the Big Foot platform is shown in Fig. 14 as a function of velocity at the two scales (Table III). Both scales are well fit by a power law with the yield proportional to v_{imp}^{8} and $S^{5.7\pm0.4}$. This is higher than the simulation-based scaling at low-yield amplification of $S^{4.4}$.[27] We postulate that the larger

TABLE I. *Hohlraum* and capsule dimensions for each of the layered implosions presented.

	Capsule dimensions (μm)								*Hohlraum* dimensions (mm)		
Shot	Inner radius	Total thickness	W (%)	Fill tube	Ice layer	Inner clean layer	Doped layer	Outer clean layer	D_H	L_H	D_{LEH}
N161030	844	63.8	0.24	10	40.5	5.4	18.5	39.9	5.4	10.13	3.46
N170109	844	65.3	0.23	10	41.0	6.3	19.9	39.2	5.4	10.13	3.46
N170524	950	72.6	0.13	5	45.6	3.4	21.4	47.9	6.0	11.3	3.9
N171015	950	72.2	0.21	5	45.4	5.7	20.9	45.7	6.0	11.3	3.9
N171029	950	72.2	0.21	5	45.3	5.8	20.8	45.6	6.0	11.3	3.9
N180128	950	72.2	0.28	5	49.4	6.3	21.4	44.5	6.0	11.3	3.9
N180909	950	72.1	0.28	5	49.6	6	21.7	44.5	6.0	11.3	3.9
N190617	844	68.3	0.24	5	44.6	6	21.8	40.5	5.4	10.13	3.46
N190721	844	68.3	0.24	5	44.5	6	21.9	40.4	5.4	10.13	3.46

TABLE II. Hotspot parameters for each of the four-layered implosions in the direct hydroscaling campaign.

	N180128	N180909	N190617	N190721
Yield	1.95×10^{16}	1.35×10^{16}	7.45×10^{15}	1.07×10^{16}
Pressure (GBar)	298 ± 16%	263 ± 16%	310 ± 16%	291 ± 16%
Y_{amp}	2.58	2.03	2.22	2.19
Bang time (ns)	8.01	7.95	7.04	7.07
P0 (μm)	30.9	28.8	22.3	27.6
P2 (μm)	0.6	−7.0	11.6	−0.6
DSR	3.04	2.93	2.98	2.94
T_{ion} (keV)	4.88 ± 0.1	4.98 ± 0.1	4.58 ± 0.1	4.83 ± 0.1
ρR (g/cm^2)	0.24	0.19	0.2	0.21
Burn width (ps)	152 ± 36	156 ± 24	131 ± 18	124 ± 18
V_{imp} (km/s)	425	427.1	423	429

size fill tubes in the smaller-scale capsule cause an apparent increase in the yield scaling as $S^{1.3}$, or ≈20%. This is consistent within error bars with other recent studies, one reporting that a 10-μm fill tube would reduce the yield by 20% when multiple degradation sources are present[29] and another reporting 40%[30] degradation relative to an implosion utilizing a 5-μm fill tube based on simulations and on two shots conducted on the NIF. The results from the initial experiments in the BigFoot platform are then consistent with the results in Sec. IV C and Appendix B that yield $\sim S^{4.5}$ at these levels of yield amplification.

B. Using the Yield Dependence of Hotspot Parameters to Infer Their Scale Dependence

In a recent study, we analyzed the velocity and yield scaling of a number of the hotspot parameters for all of the larger-scale *Hohlraum* implosions (6×11.13 mm^2 *Hohlraums* with 950-μm I.R. capsules) performed in this platform from May 2017 to September 2018 as detailed in Ref. 10. The yield scaling for each of these hotspot parameters is listed in Table IV. By simply substituting in the scaling of yield with the scale factor determined in Sec. IV, we can then arrive at the scaling of each of these hotspot parameters with scale, which we have included in Table IV along with the analytic scaling[18] of these parameters assuming the alpha heating is balancing the losses(appropriate for $1.5 \leq Y_{amp} \leq 2$).

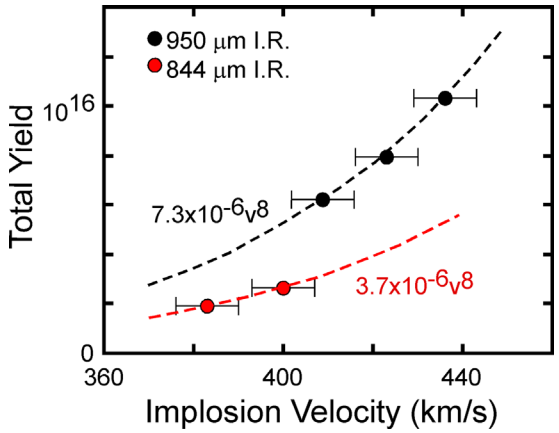

FIG. 14. Yield vs velocity of the initial five-layered implosions carried out in the BigFoot platform at S = 1 (red points) and S = 1.125 (black points). Both sets of data fit with a Y α S^8 power law.

As seen in the table, the scalings derived in this manner are on average within ∼40% of the analytic scalings; however, most of the experiments were at a higher yield amplification, $2 \leq Y_{amp} \leq 2.9$, and as such, one would expect a higher power scaling at larger yield amplification until the yield amplification starts to saturate.

VI. COMPARING THE BEST-PERFORMING IMPLOSIONS ACROSS FIVE SEPARATE SCALES

This section examines the best-performing HDC ablator implosions conducted at five distinct scales.[10,13,31–35] Because the design adiabat changed between shots at different scales and details of the laser pulse shape, these implosions are not strict hydroscales of each other. Figure 15(a) shows the laser pulse shape for each of the five implosions. The two higher adiabat implosions, N190721 and N180128 at $\alpha = 4$, were the only two implosions designed to be hydroscales of each other. The remaining three pulse shapes (N170827, N210220, and N210207) are at a lower design adiabat, $\alpha \sim 2.5$. Figure 15(b) shows the radiation temperature driven by each of the five implosions. Although the laser pulse shapes and *Hohlraum* wall materials and sizes changed between these different implosions, the combination of these changes maintained the peak radiation temperature in all of these implosions at ∼300 eV.

TABLE III. Hotspot parameters for each of the initial five-layered implosions carried out in the BigFoot campaign.

	N161030	N170109	N170524	N171015	N171029
Yield	1.85×10^{15}	2.62×10^{15}	6.22×10^{15}	7.96×10^{15}	1.03×10^{16}
Pressure (GBar)	156 ± 16%	214 ± 16%	222 ± 16%	250 ± 16%	322 ± 16%
Y_{amp}	1.38	1.45	1.73	1.88	1.96
Bang time (ns)	7.23	7.25	7.88	7.95	7.79
P0 (μm)	24.4	22.4	27.7	26.5	24.2
DSR	2.61	2.81	2.88	2.93	3.02
Tion (keV)	4.14 ± 0.1	4.16 ± 0.1	4.45 ± 0.1	4.68 ± 0.1	4.81 ± 0.1
rhoR (g/cm^2)	0.12	0.14	0.17	0.18	0.2
Burn width (ps)	138 ± 18	135 ± 36	138 ± 18	146 ± 24	143 ± 18
V_{imp} (km/s)	388.3	392.2	412.6	418.7	435.5

TABLE IV. Yield and velocity scaling fit to the database of hotspot parameters for the BigFoot platform-layered implosions shot at full scale, $6 \times 11.3\,\text{mm}^2$ *Hohlraum* and a 950-μm I.R. HDC capsule. This table also shows the hotspot parameter scaling with scale, S, given the substitution of the dependence of yield on scale along with the analytic scaling.

Hotspot parameter	Velocity and yield scaling	Experimental scaling ass. $Y \propto S^{4.4}$	Analytic scaling $Y_{amp} < 2$
Yield amplification, Y_{amp}	$v^{-0.59}Y^{0.4\pm0.16}$	$S^{1.8\pm0.7}$	$S^{1.25}$
Hotspot areal density, ρR	$v^{-0.1}Y^{0.22\pm0.04}$	$S^{1.0\pm0.18}$	$S^{2/3}$
Ion temperature, T_{ion}	$v^{1.74}Y^{0.027\pm0.04}$	$S^{0.12\pm0.18}$	$S^{1/3}$
Hotspot radius, P_0	$v^{-4.1}Y^{0.3\pm0.1}$	$S^{1.3\pm0.44}$	S
Burn width, τ_{bw}	$v^{-1.98}Y^{0.15\pm0.24}$	$S^{0.7\pm1.1}$	S
$R_{ds}-P_0$	$v^{3.1}Y^{-0.31\pm0.09}$	$S^{-1.4\pm0.4}$	
Hotspot mass, M_{hs}	$v^{-7.8}Y^{0.8\pm0.17}$	$S^{3.5\pm0.7}$	$S^{2.7}$
Hotspot pressure, P_{hs}	$v^{5.4}Y^{-0.0\pm0.16}$	$S^{0\pm0.7}$	S^0
Hotspot energy, E_{hs}	$v^{-6.1}Y^{0.83\pm0.17}$	$S^{3.7\pm0.7}$	S^3
Ignition parameter, χ_α	$v^{-0.2}Y^{0.35\pm0.16}$	$S^{1.54\pm0.7}$	$S^{1.55}$
Yield			$S^{4.4-4.7}$

A. Capulse Mass Scaling of the Best-Performing Implosions

Figure 16 shows that the initial capsule mass for the five separate implosions fairly well matches the ideal mass scaling $\sim S^{2.6}$ per 2D radiation hydrodynamics codes. Plotted also in Fig. 16 is the effective dopant areal density, ρR, for each of the five scales. According to the hydroscaling rules used in Sec. IV, the dopant concentration should decrease as S^{-1} as the dopant layer thickness increases so that the dopant ρR remains constant. This was not the case with two of the three lower adiabat implosions, which have considerably higher effective dopant concentration than the other three implosions. The implosion with the highest dopant ρR performed best, given its scale size, and had the highest DSR of the five implosions.

B. Performance as a Function of Scale

Plotting these five shots together as a function of scale vs yield enables us to compare the experimental performance with hydroscaling simulations over the five experimental scales and extrapolate the performance to larger scales. This is captured in Fig. 17(a) where the two high adiabat shots are shown as red circles and the three low-design adiabat shots are shown as black circles. The dashed lines represent two-dimensional radiation hydrodynamic hydroscaling simulations based on the high-design adiabat shot, N180128. This model adds preheat energy to the ice layer a few hundred picoseconds before the time of peak implosion velocity (over a period of 100 ps). This is designed to change the adiabat just before the deceleration phase and not affect the shock timing. It does not change the peak implosion velocity, but it does change the fuel compressibility and convergence ratio, enabling a better match to the experimental data. The dashed black line represents the design adiabat of 4 with no preheat added to the implosion. The dashed blue line represents an adiabat of 4.9 with 3.2 MJ/g added to the ice layer, and the dashed green line represents an adiabat of 5.4 with 5.4 MJ/g added to the ice. The red dashed line,

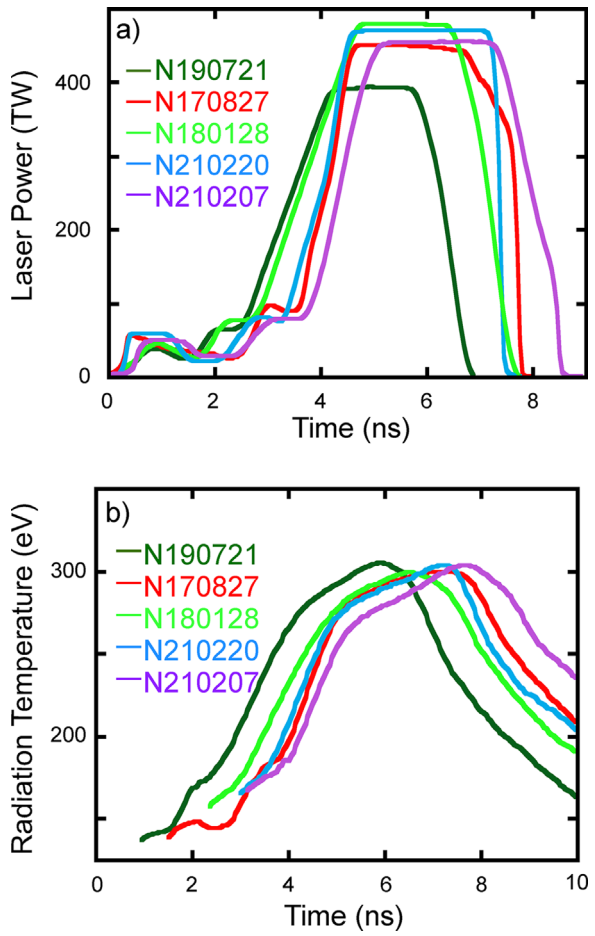

FIG. 15. (a) Laser power and (b) measured radiation temperature as a function of time for the five best-performing implosions at each capsule radius.

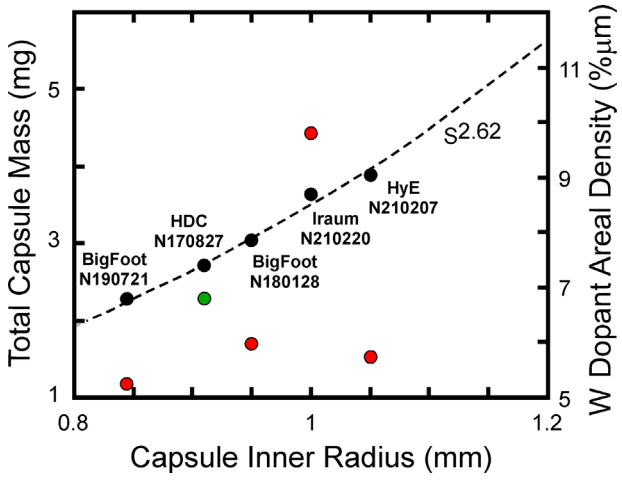

FIG. 16. Total capsule mass (black points) and dopant areal density (red points) as a function of radius for each of the best performing implosions. Black points fit to the $S^{2.6}$ power law from simulations.

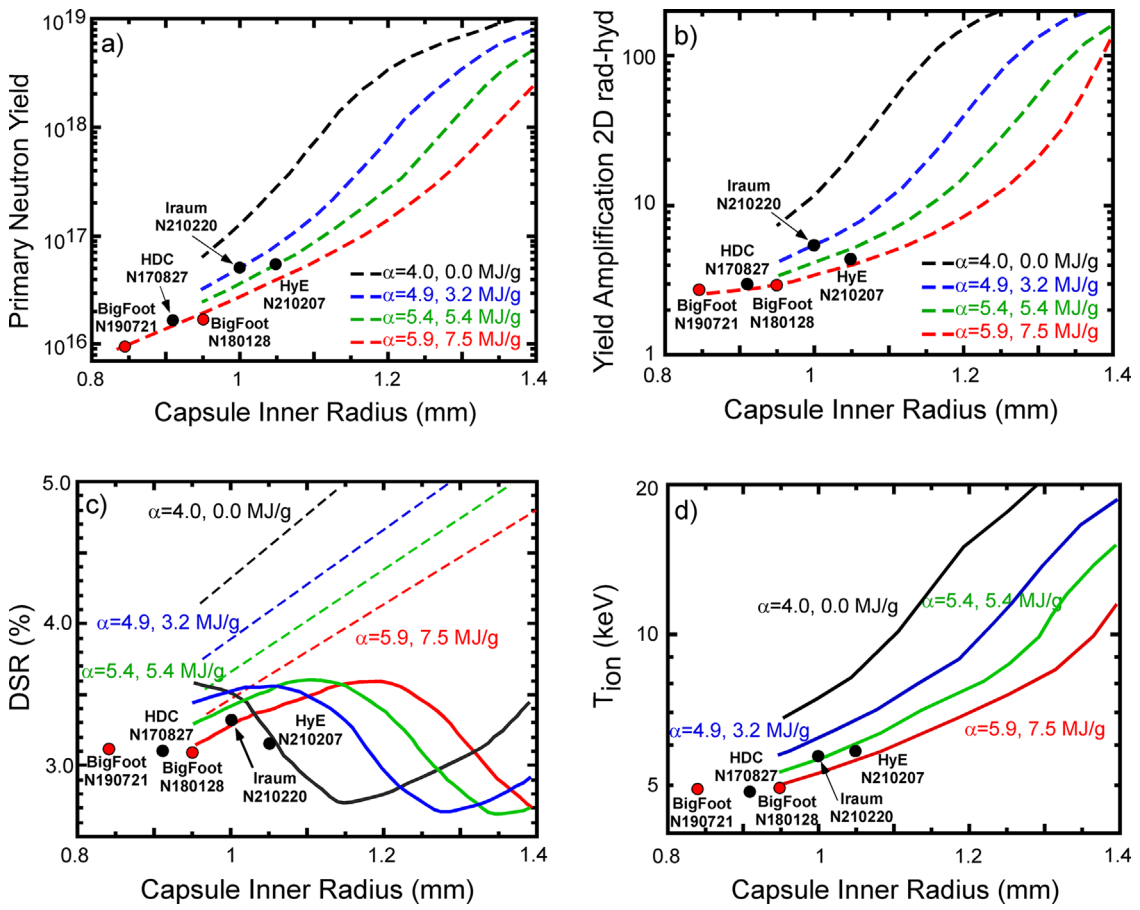

FIG. 17. Measured (points) and simulated (lines) (a) yield, (b) yield amplification, (c) neutron downscattered ratio, and (d) ion temperature as a function of capsule radius at four different adiabats. In (c), the dashed lines represent the neutron down-scattered ratio without alpha heating and the solid lines with alpha heating.

$\alpha = 5.9$, represents a good fit to the lowest three scales and a reasonable fit to the largest scale as well. The shot N210220, whose capsule contained the highest dopant areal density, is performing at the lowest adiabat of the five shots but still far above its design adiabat. The yield amplification is then shown in Fig. 17(b), where again the hydroscaled simulation with adiabat 5.9, red dashed line, provides a good fit to four of the implosions with the shot N210220 performing at a slightly lower adiabat, 4.9. Figure 17(c) represents the experimental measurements of the down-scattered ratio, DSR, that is a measure of the DT areal density at bang time, compared with hydrodynamic simulations with alpha heating, solid lines, and without alpha heating, dashed lines. The DSR for these five implosions across the five different scales remains fairly constant, differing by only 7% even though the initial ice layer thickness varied from 40 to 65 μm, a difference of 63%. This presents the largest discrepancy between experimental results and simulation expectations. If the DSR does not increase, a large burn-up fraction of the DT ice would not be achievable. Figure 17(d) represents the experimental measurements of the ion temperature compared with hydrodynamic simulations. Again, these implosions are fit fairly well with the adiabat 5.9 simulations, with N210220 operating at a slightly lower adiabat. Though these implosions were not explicitly designed to be hydroscales of each other, their performance agrees well with hydroscaling simulations, except for the DSR scaling, and indicates that all of the implosions are operating at a much higher adiabat than they were originally designed to operate at.

VII. INCREASING THE YIELD THROUGH HYDROSCALING ON THE NIF

Hydroscaling upward both the capsule and *Hohlraum* as one system takes a significant amount of laser energy and power as these parameters scale as $\sim S^{2.6}$ and $S^{1.6}$, respectively. The implosions of interest are already at the power and energy limits of the NIF laser. One way to stay within the energy and power restrictions of the NIF laser is to reduce the losses in the *Hohlraum* driving the implosion (e.g., increasing the albedo of the walls, reducing the laser entrance hole diameters, and/or reducing the *Hohlraum* wall area) in order to allow a hydroscale of the implosions to a larger capsule scale.[36] If the hydroscaling was performed in a Frustraum[37] geometry of a smaller area-to-volume ratio, the wall area can be significantly reduced from the standard cylindrical *Hohlraums* while at the same time maintaining the *Hohlraum* case-to-capsule ratio (CCR), the diameter of the *Hohlraum* divided by the outer diameter of the capsule. In addition,

the CCR can be reduced some as long as symmetry control can be maintained, by scaling up the capsule, but not the *Hohlraum*. Both approaches require further increasing the drive to compensate for the additional capsule losses associated with the larger capsule. Appendix C quantifies the power balance between the cylinder and Frustraum geometry.

The inset of Fig. 18 shows a schematic of the Iraum[38] used to drive N210220 along with a 0.85 scale Frustraum and their respective wall areas. In this case, the Frustraum has both a reduced wall area and LEH size relative to the Iraum. Figure 18 also shows the radiation temperature, dashed lines, and laser pulse shape, solid lines, from N210220 along with a proposed laser pulse shape and radiation temperature from a 2D radiation hydrodynamic simulation of the Frustraum, both hydroscaled in time. This figure shows that with the reduced area of the proposed Frustraum, the NIF laser can drive a 1.2× hydroscaled capsule, equivalent to a 1.2-mm inner radius HDC ablator. As shown in Fig. 17(b), the yield amplification from N210220 was determined to be 5.7, and hydroscaling to a 1.2-mm I.R. capsule along the same adiabat would push the yield amplification up to ∼40. Figure 19 shows the required wall area sizes for a cylinder or a Frustraum, assuming a 3.1-mm LEH, to hydroscale an implosion from a 1050-μm IR capsule driven by a 6.4-mm-diameter, 11.24-mm-long cylindrical *Hohlraum* also equipped with a 3.1-mm LEH.

Another important point to consider in hydroscaling is the Legendre mode 2 (P_2) intrinsic asymmetry imposed by the choice of *Hohlraum* geometry and hence laser illumination pattern. In order to predict the expected P_2 asymmetry of a hydroscaled capsule in a Frustraum, we have taken the empirical approach described in Refs. 39 and 40 for cylindrical *Hohlraums* and applied it to eight previous Frustraum-based implosions. These previous experiments include two Frustraum sizes, 9.26 and 7 mm in diameter, and two capsule sizes, inner radii of 12 and 1.05 mm, respectively. This model includes the sensitivity of the measurable x-ray hotspot P_2 asymmetry to capsule scale S, outer beam picket energy $E_{OutPick}$, outer beam laser spot area at the wall A, *Hohlraum* gas-fill density ρ, pulse duration τ, and the initial outer capsule radius r_{cap}. The data and physics motivated X-axis parameter used in Fig. 20(a) is $(E_{OutPick}/A/\rho)^{0.5}(\tau/R_{hohl'})(r_{cap}/R_{hohl})$

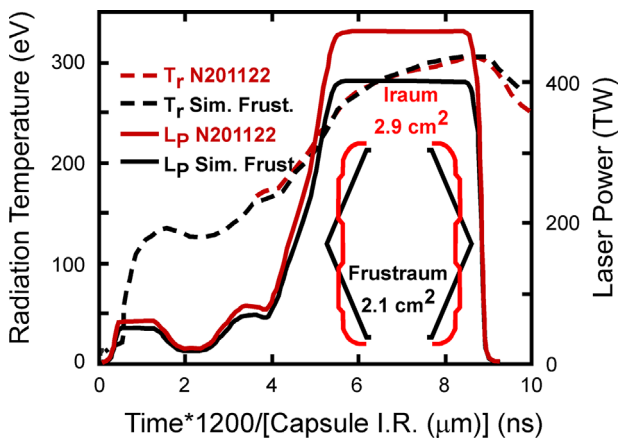

FIG. 18. Measured laser power (solid lines) and radiation temperature (dashed lines) for Iraum N201122 in red and Lasnex simulation of a 0.85 scale Frustraum in black vs scaled time. Inset shows *Hohlraum* cross sections and wall area.

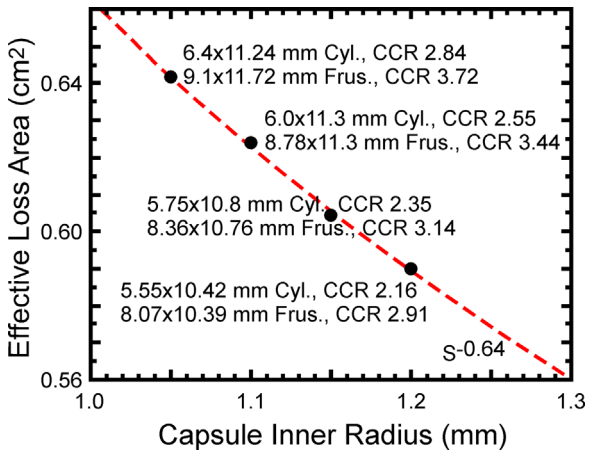

FIG. 19. *Hohlraum* wall area (and dimensions) required to hydroscale between 1050 and 1200-μm inner radius for fixed laser entrance hole diameter of 3.1 mm and fixed absorbed laser energy and power.

and for a more recent update used in Fig. 20(b) is $(E_{OutPick}/A)^{0.5}\rho^{0.13}(\tau/R_{hohl'})^{2.5}(r_{cap}/R_{hohl})^{1.1}$. In this expression for a Frustraum, $(r_{cap}/R_{hohl'})$ is the initial outer radius of the capsule divided by the radius of the wall closest to the capsule (at 23° from the equator for a 23° wall) and $(\tau/R_{hohl'})$ is the length of the laser pulse divided by the average of the wall radius where the centroid of the 44° and 50° beams hits the wall. The blue and green points in Fig. 20 are the 9.26- and 7-mm-diameter Frustraum, respectively, with a 1.2- and 1.05-mm inner radius HDC capsule, respectively. The points are well fit by a single line that is equivalent to the slope found for cylindrical implosions. The red points for a *Hohlraum* fill gas of 0.3 and 0.6 mg/cm^3 then represent the expected core symmetry of the black pulse shape in Fig. 19 driving a hydroscaled 1.2-mm inner radius HDC capsule in the 8-mm-diameter Frustraum as shown in Fig. 19. The P_2 asymmetry of both of these points should be amenable to setting to near 0 using cross-beam energy transfer, resulting from a small amount of wavelength separation, $\Delta\lambda < 2$ Å, applied between the inner and outer beams. For comparison, the anticipated $\Delta\lambda$ required for reduced size cylinders to maintain a round implosion, again using the techniques in [39,40], is shown in Table V, estimated at >6 Å for a 1.2-mm inner radius HDC capsule.

VIII. SUMMARY

The ultimate goal for indirect-drive inertial confinement fusion is to achieve high gain. One approach to increasing the yield of existing implosions is hydrodynamic scaling upward of current experiments. This approach likely represents the lowest physics risk to extrapolating yield to higher fusion energies because it does not rely on improving compression, adiabat, or implosion velocity. In this study, we presented experimental results from hydroscaling of the BigFoot design, both the *Hohlraum* and capsule, between two scales with a 12.5% difference. In addition, we also presented BigFoot data from two scales that were not direct hydroscales but had the same design adiabat and used the same platform. Both approaches gave quantitatively similar results for the scaling of yield with scale factor, S, of $Y \propto S^{4.4}$ to $S^{4.5}$, over the range of yield amplification present in those experiments, ≤2.9. By using our

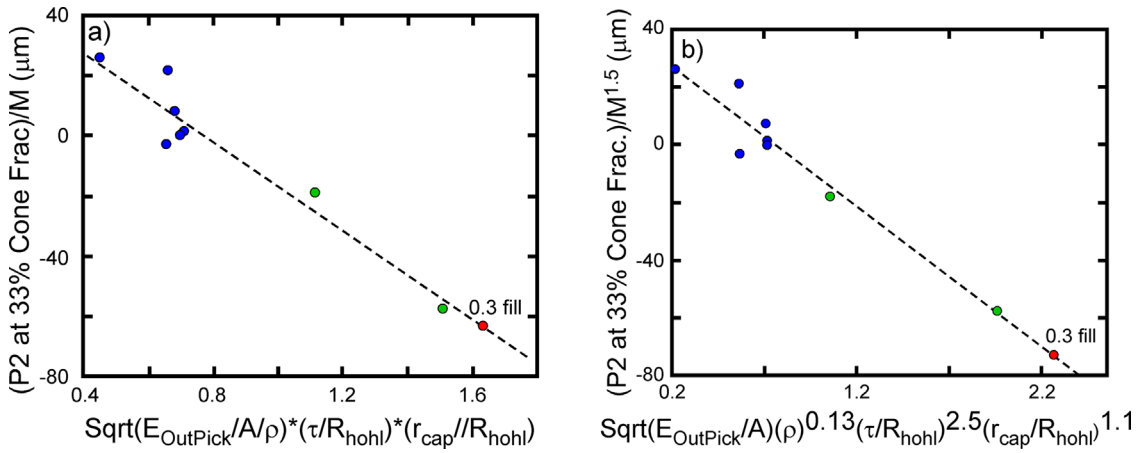

FIG. 20. Empirical fit based on (a) Ref. 39 and (b) Ref. 40 of the existing Frustraum Legendre mode 2 symmetry database. The blue and green points are the 9.26- and 7-mm-diameter Frustraums driving a 1.2- and 1.05-mm inner radius HDC capsule, respectively. The red points represent the expected core symmetry of the black pulse shape in Fig. 19 driving a 1.2-mm inner radius HDC capsule in the 8-mm-diameter Frustraum shown in Fig. 19. For the green points, M = (1.05/1.2), and for the red points, M = 1.

TABLE V. *Hohlraum* loss area required to hydroscale to a given capsule scale. The corresponding cylindrical *Hohlraum* dimensions and Frustraum dimensions are given along with the expected range of cone wavelength separation at 1ω required for the cylindrical *Hohlraum* to control P2 during the implosion.

Capsule size (μm)	Loss area (cm^2)	Frustraum dimensions (mm)	Cylinder dimensions (mm)	Expected $\Delta\lambda$ (A) for P2 control (cylinder)
1050	0.642	9.1 × 11.72	6.4 × 11.24	1.8
1100	0.624	8.78 × 11.3	6.0 × 11.3	2.9–4
1150	0.604	8.36 × 10.76	5.75 × 10.8	4–5.5
1200	0.587	8.07 × 10.39	5.55 × 10.42	5.7–9.6

previously determined scaling of hotspot parameters with yield, we were able to then obtain the scale dependence of other hotspot parameters with the scale factor S.

In addition, we compared BigFoot to three other highest-performing HDC-based implosions representing five distinct scales, different laser pulse shapes, *Hohlraum* wall materials, and design adiabat. However, the comparison was justifiable given that these designs used a very similar peak radiation temperature profile and adhered to the hydroscaled capsule initial mass scaling $S^{2.6}$. We find a good fit across these shots for yield, yield amplification, and ion temperature scaling. One shot had a slightly higher performance at its scale than the other four implosions attributed to the higher dopant areal density in its capsule. The inferred stagnated areal density for these five implosions, however, remains fairly constant, as found in other campaigns.[41] If the areal density cannot be increased beyond the linear increase that scale provides, then it would be difficult to increase the burn efficiency of these implosions required to reach high gains.

To hydroscale to higher equivalent energy and power on the NIF, the *Hohlraum* losses must be reduced. We show that by using a *Hohlraum* design with a reduced loss area, a cylinder, or a Frustraum, the existing NIF laser can drive a +20% hydroscaled version of its highest-performing implosion N210220, which according to hydroscaling simulations would result in a yield amplification ~40. We also show that the symmetry of these implosions if performed in a Frustraum should be controllable with modest amounts of cross-beam energy transfer, based on empirical fits to the symmetry of eight previous Frustraum experiments. This would also allow the case-to-capsule radius ratio to be maintained for better clearance of the inner beams.

ACKNOWLEDGMENTS

We wish to thank the NIF operations team. This paper was prepared by LLNL under Contract No. DEAC52–07NA27344. This document was prepared as an account of the work sponsored by an agency of the United States government. Neither the United States government nor Lawrence Livermore National Security, LLC, nor any of their employees make any warranty, expressed or implied, or assume any legal liability or responsibility for the accuracy, completeness, or usefulness of any information, apparatus, product, or process disclosed, or represents that its use would not infringe privately owned rights. Reference herein to any specific commercial product, process, or service by trade name, trademark, manufacturer, or otherwise does not necessarily constitute or imply its endorsement, recommendation, or favoring by the United States government or Lawrence Livermore National Security, LLC. The views and opinions of the authors expressed herein do not necessarily state or reflect those of the United States government or Lawrence Livermore National Security, LLC, and shall not be used for advertising or product endorsement purposes.

AUTHOR DECLARATIONS

Conflict of Interest

The authors have no conflicts to disclose.

DATA AVAILABILITY

The data that support the findings of this study are available from the corresponding author upon reasonable request.

APPENDIX A: BIGFOOT IMPLOSION DESIGN

The hydroscale campaign was conducted using the BigFoot platform, which was developed at the National Ignition Facility to study inertial confinement fusion in a platform that attempted to minimize deleterious plasma physics effects and reduce hydrodynamic instabilities.[2,10,12–15] The *Hohlraums* at both scales were filled with helium gas at 0.3 mg/cm^3. A gas fill, >0.03 mg/cm^3, is required to provide sufficient heat conduction to enable the production of the ice layer inside the capsule. The 0.3 mg/cm^3 gas fill that was fielded on the BigFoot platform minimized the impact of laser-plasma instabilities associated with higher gas-fill densities and yet was high enough to partially tamp the expansion of *Hohlraum* wall and ablator material into the laser beam paths that have been problematic at the lower gas-fill density, 0.03 mg/cm^3. The two outer beam cones were separated along the length of the *Hohlraum*, denoted cone splitting, and the four beams comprising an individual quad were separated into two groups of two beams separated in azimuth with each group containing two orthogonally polarized beams, denoted quad splitting. These changes were made to reduce the intensity on the wall and to, therefore, help reduce stimulated Brillouin. A key advantage of the HDC ablators used in this platform is the higher density and sound speed, both about 3× higher as compared to CH ablators.[42–44] The high laser intensities where the outer laser beams intersect the *Hohlraum* wall drive a gold bubble that expands toward the axis of the *Hohlraum* and can eventually begin to absorb the inner beams for sufficiently long laser pulses, thereby removing symmetry drive control of the implosion. The higher density in the HDC ablators enables much shorter laser pulse lengths with less complications from the gold bubble expansion than in CH-based ICF platforms with much longer pulse lengths. The beam intensity reduction resulting from the cone and quad splitting also reduced the bubble expansion of the wall.

The pulse shape for the platform was also designed to minimize instability issues with the capsules. The pulse shape was a three-shock design with the foot power set to launch a first shock of at least 12 Mbar to avoid refreezing of the carbon and the seeding of nonuniformities after shock transition.[42,45] Shocks one and two were timed to merge a few μm before the inner ablator–ice interface. The merged first and second shocks are then timed to merge with the third shock a few μm after the inner ice–gas interface. This had the effect of sending three shocks through the ablator, and only two shocks through the ice such that the ablator density remained higher than the ice density and, therefore, maintained a stable, negative, Atwood number at peak implosion velocity. Two-dimensional capsule-only simulations indicate that this pulse shape, in the simulations at least, produces the most stable implosion of all the ICF campaigns that have been conducted on the NIF using HDC ablators.[46]

APPENDIX B: VELOCITY-CORRECTED YIELD SCALING

The inferred and measured hotspot parameters for the entire BigFoot campaign can also be used to estimate the relative velocity between the pairs of shots as mentioned above. Our previous study on the larger-scale implosions showed that when the hotspot parameters were expressed in terms of velocity and yield that the hotspot parameters collapsed to a single power law as a function of velocity.[10] By plotting velocity vs the hotspot parameter with the yield dependence removed, an effective velocity can be determined. Figure 21 shows five different hotspot parameters, with their yield dependence removed, for all of the BigFoot platform-layered implosions through N190721 plotted as a function of postshot velocity, except for the four hydroscaling implosions N180128, N180909, N190617, and N190721. The four hydroscaling implosions are evaluated for the hotspot parameter and placed on the fit of the remaining shots conducted on the BigFoot platform to estimate their velocity. In particular, the hotspot pressure is shown in Fig. 21(a), the hotspot radius in Fig. 21(b), the hotspot energy in Fig. 21(c), the hotspot mass in Fig. 21(d), and the ion temperature in Fig. 21(e). The average inferred velocities from the five plots for the four shots were 433 for N190617, 429 for N190721, 434 for N180909, and 435 km/s for N180128. That implied that N190721 was 5 km/s slower than N180128 and N190617 was 1 km/s slower than N180909. The corrected yield ratio for these pairs would then be $1.95 \times 10^{16}[(434.7–4.97)/434.7]^{10}/1.07 \times 10^{16} = 1.62$. The ratio of the total yields for the second full scale and subscale pair, N180909 and N190617, is then $1.35 \times 10^{16}[(433.9 - 1.1)/433.9]^{10}/7.45 \times 10^{15} = 1.77$. Averaging these two results together implies an average yield ratio of 1.7 or a yield dependence on the scale factor, S, of $Y \propto S^{4.5}$.

APPENDIX C: *HOHLRAUM* POWER BALANCE, CYLINDER VERSUS FRUSTRAUM GEOMETRY

The peak temperature in a *Hohlraum* can be approximated as a power balance between the x-ray power produced in the *Hohlraum* and the x-ray power lost to the walls of the *Hohlraum*, the capsule itself, and the laser entrance holes.[47,48] The x-ray power produced in the *Hohlraum* is simply the laser power, P_L, entering the laser entrance holes multiplied by the conversion factor of laser power into x rays, β. The power lost to the walls is the x-ray flux inside the *Hohlraum*, σT_r^4 multiplied by the wall area, A_w, and the factor $(1-\alpha_w)$, which denotes the fraction of the x-ray power that enters the *Hohlraum* walls and is lost to the cavity, where α_w is the wall albedo. The power lost to the capsule is the x-ray flux inside the *Hohlraum* multiplied by the surface area of the capsule and the factor $(1-\alpha_c)$, which denotes the fraction of the x-ray power that enters the capsule, where α_c is the capsule albedo. The x-ray power lost to the laser entrance holes is simply the x-ray flux inside the *Hohlraum* multiplied by the surface area of the laser entrance holes. The power balance is then

$$\beta P_L = \sigma T_r^4 \left[A_w(1-\alpha_w) + 4\pi R_c^2(1-\alpha_c) + 2\pi R_{LEH}^2\right], \quad \text{(C1)}$$

with the effective loss area equal to $\left[A_w(1-\alpha_w) + 4\pi R_c^2(1-\alpha_c) + 2\pi R_{LEH}^2\right]$. The wall area of a cylindrical *Hohlraum*, A_{CH}, with a radiused end, R_{cur}, is simply

$$A_{CH} = 2\pi R_{CH}(L_{CH} - 2R_{cur}) + 2\pi\left((R_{CH} - R_{cur})^2 - R_{LEH}^2\right) + 2\left(\pi^2 R_{CH} R_{cur} - \pi R_{cur}^2(\pi - 2)\right). \quad \text{(C2)}$$

The wall area of a Frustraum *Hohlraum*, A_{FH}, with walls at an angle of θ is given by

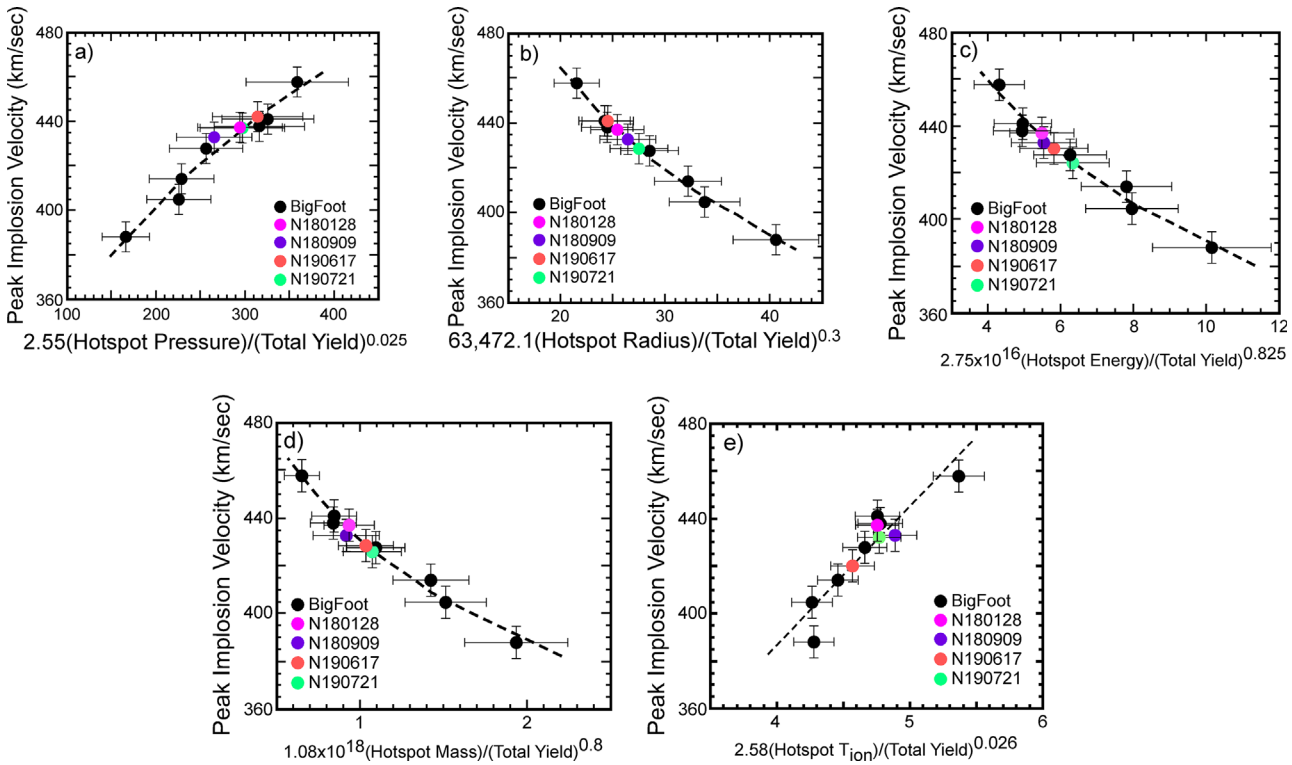

FIG. 21. Hotspot parameters (a) pressure, (b) radius, (c) energy, (d) mass, and (e) ion temperature for all of the BigFoot platform-layered implosions through N190721 plotted as a function of postshot velocity and the hotspot parameter with its yield dependence removed, except for the four-layered implosions comprising the direct hydroscaling implosions.

$$A_{FH} = 2\pi\left(R_{FHe}^2 - R_{FHp}^2\right)/\sin(\theta) + 2\pi\left(R_{FHp}^2 - R_{LEH}^2\right). \quad \text{(C3)}$$

The power ratio, P_{Lratio}, of the laser required to drive the same temperature profile in the respective *Hohlraums* is then

$$P_{Lratio} = \frac{2\pi R_{LEH\_CH}^2 + 4\pi(1-\alpha_{CAP})R_{CAP}^2 + (1-\alpha_W)A_{CH}}{2\pi R_{LEH\_F}^2 + 4\pi(1-\alpha_{CAP})R_{CAP}^2 + (1-\alpha_W)A_{FH}}. \quad \text{(C4)}$$

To estimate the needed power and energy required to drive a hydroscale of a given implosion, the capsule and the *Hohlraum* are first scaled up by a factor S. The laser power to drive such a scale-up has the power increased by $S^{1.6}$ and the time stretched by the factor S, hence energy increased by $S^{2.6}$. This would then drive a radiation temperature in this scaled target that is scaled in time by the factor S relative to the initial implosion. The power needed for the reduced loss area *Hohlraum* to drive the same radiation temperature is then the scaled-up power profile divided by the ratio of the effective *Hohlraum* loss area of the new *Hohlraum* to that of the hydroscaled *Hohlraum*. The capsule size between these two *Hohlraums* would remain constant. As a specific example, if the target in N210220 was hydroscaled up by 20%, the capsule inner radius would increase from 1 mm to 1.2 mm. The peak laser power would increase from 471 TW to $455 \times (1.2)^{1.6} = 631$ TW and the laser energy from 1.79 MJ to $1.79 \times (1.2)^{2.6} = 2.88$ MJ. N210220 used a cylindrical *Hohlraum,* which had a wall area of 2.9 cm^2 and an LEH that was 3.64 mm in diameter. The effective wall loss area of the original *Hohlraum* with a 1-mm inner radius capsule was 0.71 cm^2. Hydroscaling that target up by 20% would result in a cylindrical *Hohlraum* with a wall area of 4.18 cm^2 and an LEH that was 4.37 mm in diameter. The effective wall loss area of the hydroscaled target with a 1.2-mm inner radius capsule would then be 1.1 cm^2. Placing that capsule into a reduced loss area *Hohlraum* of 0.59 cm^2 (say a 5.55×10.42 mm^2 cylindrical *Hohlraum* or an 8.07×10.39 mm^2 Frustraum, both with 3.11-mm-diameter LEHs) would then enable a reduction of the peak power of the hydroscaled target of 0.59/1.1 or a 1.58× reduction. The reduced loss area *Hohlraum* then could drive the same radiation temperature for a 1.2-mm inner radius capsule with a peak power of 631 TW/1.58 = 399 TW and a laser energy of 2.88 MJ/1.58 = 1.83 MJ, both within the laser and power limits of the NIF. More examples, both cylinders and Frustraum, are given in Fig. 19 keeping the *Hohlraum* wall material and LEH diameter constant.

REFERENCES

[1]J. D. Lindl, O. L. Landen, J. Edwards, E. I. Moses, J. Adams, P. A. Amendt, N. Antipa, P. A. Arnold, L. J. Atherton, S. Azevedo, D. Barker, M. A. Barrios, I. Bass, S. H. Baxamusa, R. Beeler, B. V. Beeman, P. M. Bell, L. R. Benedetti, L. Bernstein, L. B. Hopkins, S. D. Bhandarkar, T. Biesiada, R. M. Bionta, D. L. Bleuel, E. J. Bond, M. Borden, M. W. Bowers, D. K. Bradley, D. Browning, G. K. Brunton, J. Bude, S. C. Burkhart, R. F. Burr, B. Butlin, J. A. Caggiano, D. A.

Callahan, A. C. Carpenter, C. W. Carr, D. T. Casey, C. Castro, J. Celeste, P. M. Celliers, C. J. Cerjan, J. Chang, M. Chiarappa-Zucca, C. Choate, T. J. Clancy, D. S. Clark, S. J. Cohen, G. W. Collins, A. Conder, J. R. Cox, P. S. Datte, G. A. Deis, E. L. Dewald, P. D. Nicola, J. M. Di Nicola, L. Divol, S. N. Dixit, T. Doeppner, V. Draggoo, O. Drury, R. Dylla-Spears, E. G. Dzenitis, J. M. Dzenitis, M. J. Eckart, D. C. Eder, J. H. Eggert, R. B. Ehrlich, G. V. Erbert, J. Fair, D. R. Farley, M. Fedorov, B. Felker, R. Finucane, A. Fisher, D. N. Fittinghoff, J. Folta, R. J. Fortner, T. Frazier, G. Frieders, S. Frieders, S. Friedrich, J. Fry, J. Gaylord, S. M. Glenn, S. H. Glenzer, B. Golick, G. Gururangan, G. Guss, S. W. Haan, B. J. Haid, B. Hammel, A. V. Hamza, E. P. Hartouni, R. Hatarik, B. W. Hatch, S. P. Hatchett, R. Hawley, C. Haynam, J. Heebner, G. Heestand, M. R. Hermann, V. J. Hernandez, D. G. Hicks, D. E. Hinkel, D. D. Ho, J. P. Holder, D. Holunga, J. Honig, J. Horner, R. K. House, M. Hutton, N. Izumi, M. C. Jackson, K. S. Jancaitis, D. R. Jedlovec, M. A. Johnson, O. S. Jones, D. H. Kalantar, R. L. Kauffman, L. Kegelmeyer, G. Kerbel, M. Key, S. F. Khan, J. R. Kimbrough, R. Kirkwood, J. J. Klingman, J. A. Koch, T. R. Kohut, J. M. Koning, K. M. Knittel, B. J. Kozioziemski, G. W. Krauter, K. Krauter, A. Kritcher, J. Kroll, W. L. Kruer, G. LaCaille, K. N. LaFortune, L. J. Lagin, T. A. Land, A. B. Langdon, S. H. Langer, D. W. Larson, D. A. Latray, T. Laurence, S. LePape, R. A. Lerche, Z. Liao, J. Liebman, R. A. London, R. R. Lowe-Webb, T. Ma, B. J. MacGowan, A. J. MacKinnon, A. G. MacPhee, T. N. Malsbury, K. Manes, A. M. Manuel, E. R. Mapoles, M. M. Marinak, C. D. Marshall, D. Mason, N. Masters, D. G. Mathisen, I. Matthews, T. McCarville, J. M. McNaney, D. J. Meeker, N. B. Meezan, J. Menapace, P. Michel, P. E. Miller, J. L. Milovich, M. Mintz, R. Montesanti, M. Monticelli, J. D. Moody, M. J. Moran, J. C. Moreno, D. H. Munro, R. A. Negres, J. R. Nelson, M. Norton, M. Nostrand, M. O'Brien, Y. P. Opachich, C. Orth, A. E. Pak, E. S. Palma, J. N. E. Palmer, T. G. Parham, H. S. Park, P. K. Patel, R. W. Patterson, J. E. Peterson, J. L. Peterson, T. Phillips, R. Prasad, K. Primdahl, S. T. Prisbrey, S. R. Qiu, J. E. Ralph, K. S. Raman, F. Ravizza, B. Raymond, B. A. Remington, M. A. Rever, J. Reynolds, M. J. Richardson, A. C. Riddle, B. Rittmann, M. D. Rosen, J. S. Ross, J. R. Rygg, R. A. Sacks, J. T. Salmon, J. D. Salmonson, J. D. Sater, R. L. Saunders, R. Sawicki, K. Schaffers, D. H. Schneider, M. B. Schneider, H. A. Scott, S. M. Sepke, R. Seugling, D. A. Shaughnessy, M. J. Shaw, R. Shelton, N. Shen, N. Shingleton, N. Simanovskaia, V. Smalyuk, D. A. Smauley, M. Spaeth, B. K. Spears, D. R. Speck, T. M. Spinka, P. T. Springer, M. Stadermann, W. Stoeffl, J. Stolken, C. Stolz, E. Storm, D. J. Strozzi, T. Suratwala, L. J. Suter, J. S. Taylor, C. A. Thomas, G. L. Tietbohl, R. Tommasini, D. Trummer, B. VanWonterghem, R. Von Rotz, R. J. Wallace, C. F. Walters, A. Wang, A. L. Warrick, S. Weaver, S. V. Weber, P. J. Wegner, K. Widmann, C. C. Widmayer, E. A. Williams, P. K. Whitman, K. Wilhelmsen, M. Witte, L. Wong, R. D. Wood, S. Yang, C. Yeamans, B. K. Young, B. Yoxall, R. A. Zacharias, G. B. Zimmerman, S. Batha, C. R. Danly, V. Fatherley, G. P. Grim, N. Guler, H. W. Herrmann, Y. Kim, J. L. Kline, G. A. Kyrala, R. J. Leeper, D. Martinson, F. E. Merrill, R. E. Olson, C. Wilde, M. D. Wilke, D. C. Wilson, G. A. Chandler, G. W. Cooper, K. D. Hahn, K. J. Peterson, C. L. Ruiz, K. C. Chen, N. Dorsano, M. Emerich, C. Gibson, D. Hoover, M. Hoppe, J. D. Kilkenny, K. Moreno, H. Wilkens, S. Woods, J. A. Frenje, M. G. Johnson, C. K. Li, R. D. Petrasso, H. Rinderknecht, M. Rosenberg, F. H. Seguin, A. Zylstra, W. Garbett, P. Graham, T. Guymer, A. S. Moore, J. L. Bourgade, P. Gauthier, J. P. Leidinger, L. Masse, F. Philippe, and R. H. H. Scott, "Review of the National Ignition Campaign 2009–2012 (vol. 21, 020501, 2014)," Phys. Plasmas **21**, 129902 (2014).

[2]K. L. Baker, C. A. Thomas, D. T. Casey, S. Khan, B. K. Spears, R. Nora, T. Woods, J. L. Milovich, R. L. Berger, D. Strozzi, D. Clark, M. Hohenberger, O. A. Hurricane, D. A. Callahan, O. L. Landen, B. Bachmann, R. Benedetti, R. Bionta, P. M. Celliers, D. Fittinghoff, C. Goyon, G. Grim, R. Hatarik, N. Izumi, M. Gatu Johnson, G. Kyrala, T. Ma, M. Millot, S. R. Nagel, A. Pak, P. K. Patel, D. Turnbull, P. L. Volegov, and C. Yeamans, "High-performance indirect-drive cryogenic implosions at high adiabat on the National Ignition Facility," Phys. Rev. Lett. **121**, 135001 (2018).

[3]R. Nora, R. Betti, K. S. Anderson, A. Shvydky, A. Bose, K. M. Woo, A. R. Christopherson, J. A. Marozas, T. J. B. Collins, P. B. Radha, S. X. Hu, R. Epstein, F. J. Marshall, R. L. McCrory, T. C. Sangster, and D. D. Meyerhofer, "Theory of hydro-equivalent ignition for inertial fusion and its applications to OMEGA and the National Ignition Facility," Phys. Plasmas **21**, 056316 (2014).

[4]I. A. B. Zelıdovich, I. U. P. Raizer, W. D. Hayes, and R. F. Probstein, *Physics of Shock Waves and High-Temperature Hydrodynamic Phenomena* (Academic Press, New York, 1966).

[5]L. J. Suter, A. A. Bauer, L. V. Powers, D. B. Ress, N. Delameter, W. W. Hsing, O. L. Landen, A. R. Thiessen, and R. E. Turner, "Modeling and interpretation of Nova's symmetry scaling data base," Phys. Rev. Lett. **73**, 2328 (1994).

[6]H. Takabe, K. Mima, L. Montierth, and R. L. Morse, "Self-consistent growth rate of the Rayleigh–Taylor instability in an ablatively accelerating plasma," Phys. Fluids **28**, 3676 (1985).

[7]J. Lindl, "Development of the indirect-drive approach to inertial confinement fusion and the target physics basis for ignition and gain," Phys. Plasmas **2**, 3933 (1995).

[8]S. Palaniyappan, J. P. Sauppe, B. J. Tobias, C. F. Kawaguchi, K. A. Flippo, A. B. Zylstra, O. L. Landen, D. Shvarts, E. Malka, S. H. Batha, P. A. Bradley, E. N. Loomis, N. N. Vazirani, L. Kot, D. W. Schmidt, T. H. Day, R. Gonzales, and J. L. Kline, "Hydro-scaling of direct-drive cylindrical implosions at the OMEGA and the National Ignition Facility," Phys. Plasmas **27**, 042708 (2020).

[9]D. S. Clark, C. R. Weber, J. L. Milovich, A. E. Pak, D. T. Casey, B. A. Hammel, D. D. Ho, O. S. Jones, J. M. Koning, A. L. Kritcher, M. M. Marinak, L. P. Masse, D. H. Munro, M. V. Patel, P. K. Patel, H. F. Robey, C. R. Schroeder, S. M. Sepke, and M. J. Edwards, "Three-dimensional modeling and hydrodynamic scaling of National Ignition Facility implosions," Phys. Plasmas **26**, 050601 (2019).

[10]K. L. Baker, C. A. Thomas, D. T. Casey, M. Hohenberger, S. Khan, B. K. Spears, O. L. Landen, R. Nora, T. Woods, J. L. Milovich, R. L. Berger, D. Strozzi, D. Clark, O. A. Hurricane, D. A. Callahan, A. Kritcher, B. Bachmann, R. Benedetti, R. Bionta, P. M. Celliers, D. Fittinghoff, C. Goyon, R. Hatarik, N. Izumi, M. Gatu Johnson, G. Kyrala, T. Ma, K. Meaney, M. Millot, S. R. Nagel, A. Pak, P. K. Patel, D. Turnbull, P. L. Volegov, C. Yeamans, and C. Wilde, "Hotspot parameter scaling with velocity and yield for high adiabat layered implosions on the National Ignition Facility," Phys. Rev. E **102**, 023210 (2020).

[11]P. K. Patel, P. T. Springer, C. Weber, L. C. Jarrott, O. A. Hurricane, B. Bachmann, K. Baker, L. B. Hopkins, D. Callahan, D. T. Casey, C. Cerjan, D. S. Clark, E. L. Dewald, L. Divol, T. Doeppner, J. E. Field, D. N. Fittinghoff, J. A. Gaffney, V. Geppert-Kleinrath, G. Grim, E. P. Hartouni, R. Hatarik, D. Hinkel, M. Hohenberger, K. Humbird, N. Izumi, O. S. Jones, S. F. Khan, A. L. Kritcher, M. K. Gerhard Kruse, O. Landen, S. Le Pape, T. Ma, S. A. MacLaren, A. MacPhee, L. P. Masse, N. Meezan, J. L. Milovich, R. Nora, A. Pak, J. L. Peterson, J. Ralph, H. F. Robey, J. D. Salmonson, V. Smalyuk, B. K. Spears, C. A. Thomas, P. Volegov, A. Zylstra, and M. John Edwards, "Hotspot conditions achieved in inertial confinement fusion experiments on the National Ignition Facility," Phys. Plasmas **27**, 050901 (2020).

[12]D. T. Casey, C. A. Thomas, K. L. Baker, B. K. Spears, M. Hohenberger, S. F. Khan, R. C. Nora, C. R. Weber, D. T. Woods, O. A. Hurricane, D. A. Callahan, R. L. Berger, J. L. Milovich, P. K. Patel, T. Ma, A. Pak, L. R. Benedetti, M. Millot, C. Jarrott, O. L. Landen, R. M. Bionta, B. J. MacGowan, D. J. Strozzi, M. Stadermann, J. Biener, A. Nikroo, C. S. Goyon, N. Izumi, S. R. Nagel, B. Bachmann, P. L. Volegov, D. N. Fittinghoff, G. P. Grim, C. B. Yeamans, M. Gatu Johnson, J. A. Frenje, N. Rice, C. Kong, J. Crippen, J. Jaquez, K. Kangas, and C. Wild, "The high velocity, high adiabat, 'Bigfoot' campaign and tests of indirect-drive implosion scaling," Phys. Plasmas **25**, 056308 (2018).

[13]C. A. Thomas, E. M. Campbell, K. L. Baker, D. T. Casey, M. Hohenberger, A. L. Kritcher, B. K. Spears, S. Khan, R. Nora, D. T. Woods, J. L. Milovich, R. L. Berger, D. Strozzi, D. D. Ho, D. Clark, B. Bachmann, R. Benedetti, R. Bionta, P. M. Celliers, D. Fittinghoff, G. Grim, R. Hatarik, N. Izumi, G. Kyrala, T. Ma, M. Millot, S. R. Nagel, P. K. Patel, C. Yeamans, A. Nikroo, M. Tabak, M. Gatu Johnson, P. L. Volegov, and S. M. Finnegan, "Deficiencies in compression and yield in x-ray driven implosions," Phys. Plasmas **27**, 112705 (2020).

[14]M. Hohenberger, D. T. Casey, C. A. Thomas, O. L. Landen, K. L. Baker, L. R. Benedetti, D. A. Callahan, O. A. Hurricane, N. Izumi, S. F. Khan, T. Ma, D. A. Mariscal, S. R. Nagel, A. Pak, and B. K. Spears, "Maintaining low-mode symmetry control with extended pulse-shapes for lower-adiabat Bigfoot implosions on the National Ignition Facility," Phys. Plasmas **26**, 112707 (2019).

[15]R. Berger, C. A. Thomas, K. Baker, D. Casey, C. Goyon, J. Park, N. Lemos, S. Khan, M. Hohenberger, J. Milovich, D. Strozzi, M. Belyaev, T. Chapman, and A. Bruce Langdon, "Stimulated backscatter of laser light from BigFoot *Hohlraums* on the National Ignition Facility," Phys. Plasmas **26**, 012709 (2019).

[16]E. L. Dewald, L. J. Suter, O. L. Landen, J. P. Holder, J. Schein, F. D. Lee, K. M. Campbell, F. A. Weber, D. G. Pellinen, M. B. Schneider, J. R. Celeste, J. W. McDonald, J. M. Foster, C. Niemann, A. J. Mackinnon, S. H. Glenzer, B. K. Young, C. A. Haynam, M. J. Shaw, R. E. Turner, D. Froula, R. L. Kauffman, B. R. Thomas, L. J. Atherton, R. E. Bonanno, S. N. Dixit, D. C. Eder, G. Holtmeier, D. H. Kalantar, A. E. Koniges, B. J. MacGowan, K. R. Manes, D. H. Munro, J. R. Murray, T. G. Parham, K. Piston, B. M. Van Wonterghem, R. J. Wallace, P. J. Wegner, P. K. Whitman, B. A. Hammel, and E. I. Moses, "Radiation-driven hydrodynamics of high-Z *Hohlraums* on the National Ignition Facility," Phys. Rev. Lett. **95**, 215004 (2005).

[17]D. A. Callahan, O. A. Hurricane, D. E. Hinkel, T. Döppner, T. Ma, H.-S. Park, M. A. Barrios Garcia, L. F. Berzak Hopkins, D. T. Casey, C. J. Cerjan, E. L. Dewald, T. R. Dittrich, M. J. Edwards, S. W. Haan, A. V. Hamza, J. L. Kline, J. P. Knauer, A. L. Kritcher, O. L. Landen, S. LePape, A. G. MacPhee, J. L. Milovich, A. Nikroo, A. E. Pak, P. K. Patel, J. R. Rygg, J. E. Ralph, J. D. Salmonson, B. K. Spears, P. T. Springer, R. Tommasini, L. R. Benedetti, R. M. Bionta, E. J. Bond, D. K. Bradley, J. A. Caggiano, J. E. Field, D. N. Fittinghoff, J. Frenje, M. Gatu Johnson, G. P. Grim, R. Hatarik, F. E. Merrill, S. R. Nagel, N. Izumi, S. F. Khan, R. P. J. Town, D. B. Sayre, P. Volegov, and C. H. Wilde, "Higher velocity, high-foot implosions on the National Ignition Facility laser," Phys. Plasmas **22**, 056314 (2015).

[18]O. A. Hurricane, D. A. Callahan, P. T. Springer, M. J. Edwards, P. Patel, K. Baker, D. T. Casey, L. Divol, T. Döppner, D. E. Hinkel, L. F. Berzak Hopkins, A. Kritcher, S. Le Pape, S. Maclaren, L. Masse, A. Pak, L. Pickworth, J. Ralph, C. Thomas, A. Yi, and A. Zylstra, "Beyond alpha-heating: Driving inertially confined fusion implosions toward a burning-plasma state on the National Ignition Facility," Plasma Phys. Controlled Fusion **61**, 014033 (2019).

[19]O. A. Hurricane, D. T. Casey, O. Landen, A. L. Kritcher, R. Nora, P. K. Patel, J. A. Gaffney, K. D. Humbird, J. E. Field, M. K. G. Kruse, J. L. Peterson, and B. K. Spears, "An analytic asymmetric-piston model for theimpact of mode-1 shell asymmetry on ICF implosions," Phys. Plasmas **27**, 062704 (2020).

[20]D. T. Casey, B. MacGowan, J. D. Sater, A. Zylstra, A. L. Kritcher, M. Hohenberger, K. Baker, S. L. Pape, T. Doeppner, C. Weber, H. Huang, O. L. Landen, J. Milovich, J. Biener, S. Haan, S. Ross, H. Robey, M. Stadermann, A. Nikroo, D. A. Callahan, O. A. Hurricane, M. Bruhn, C. Kong, K. Sequoia, N. Rice, and C. Wild, "Evidence of three-dimensional asymmetries seeded by HDC-ablator non-uniformity in experiments at the National Ignition Facility," Phys. Rev. Lett. **126**, 025002 (2021).

[21]J. Milovich, D. Casey, B. MacGowan, D. Clark, D. Mariscal, T. Ma, K. Baker, R. Bionta, K. Hahn, A. Moore, D. Schlossberg, E. Hartouni, S. Sepke, and O. Landen, "Understanding asymmetries using integrated simulations of capsule implosions in low gas-fill *Hohlraums* at the National Ignition Facility," Plasma Phys. Controlled Fusion **63**, 025012 (2021).

[22]D. L. Bleuel, C. B. Yeamans, L. A. Bernstein, R. M. Bionta, J. A. Caggiano, D. T. Casey, G. W. Cooper, O. B. Drury, J. A. Frenje, C. A. Hagmann, R. Hatarik, J. P. Knauer, M. G. Johnson, K. M. Knittel, R. J. Leeper, J. M. McNaney, M. Moran, C. L. Ruiz, and D. H. G. Schneider, "Neutron activation diagnostics at the National Ignition Facility," Rev. Sci. Instrum. **83**, 10D313 (2012).

[23]C. B. Yeamans and D. L. Bleuel, "The spatially distributed neutron activation diagnostic FNADs at the National Ignition Facility," Fusion Sci. Technol. **72**, 120 (2017).

[24]D. G. Hicks, B. K. Spears, D. G. Braun, R. E. Olson, C. M. Sorce, P. M. Celliers, G. W. Collins, and O. L. Landen, "Convergent ablator performance measurements," Phys. Plasmas **17**, 102703 (2010).

[25]R. E. Olson, G. A. Rochau, O. L. Landen, and R. J. Leeper, "X-ray ablation rates in inertial confinement fusion capsule materials," Phys. Plasmas **18**, 032706 (2011).

[26]Y. Saillard, "Acceleration and deceleration model of indirect drive ICF capsules," Nucl. Fusion **46**, 1017 (2006).

[27]D. A. Callahan, O. A. Hurricane, A. L. Kritcher, D. T. Casey, D. E. Hinkel, Y. P. Opachich, H. F. Robey, M. D. Rosen, J. S. Ross, M. S. Rubery, C. V. Young, and A. B. Zylstra, "A simple model to scope out parameter space for indirect drive designs on NIF," Phys. Plasmas **27**, 072704 (2020).

[28]K. L. Baker, C. A. Thomas, T. R. Dittrich, O. Landen, G. Kyrala, D. T. Casey, C. W. Mauche, C. R. Weber, J. Milovich, D. T. Woods, M. Schneider, S. F. Khan, B. K. Spears, C. Kong, J. Crippen, N. Alfonso, C. B. Yeamans, J. D. Moody, A. S. Moore, N. B. Meezan, A. Pak, D. N. Fittinghoff, P. L. Volegov, O. Hurricane, D. Callahan, P. Patel, and P. Amendt, "Fill tube dynamics in inertial confinement fusion implosions with high density carbon ablators," Phys. Plasmas **27**, 112706 (2020).

[29]C. R. Weber, D. S. Clark, A. Pak, N. Alfonso, B. Bachmann, L. F. Berzak Hopkins, T. Bunn, J. Crippen, L. Divol, T. Dittrich, A. L. Kritcher, O. L. Landen, S. L. Pape, A. G. MacPhee, E. Marley, L. P. Masse, J. L. Milovich, A. Nikroo, P. K. Patel, L. A. Pickworth, N. Rice, V. A. Smalyuk, and M. Stadermann, "Mixing in ICF implosions on the National Ignition Facility caused by the fill-tube," Phys. Plasmas **27**, 032703 (2020).

[30]A. Pak, L. Divol, C. R. Weber, L. F. Berzak Hopkins, D. S. Clark, E. L. Dewald, D. N. Fittinghoff, V. Geppert-Kleinrath, M. Hohenberger, S. L. Pape, T. Ma, A. G. MacPhee, D. A. Mariscal, E. Marley, A. S. Moore, L. A. Pickworth, P. L. Volegov, C. Wilde, O. A. Hurricane, and P. K. Patel, "Impact of localized radiative loss on inertial confinement fusion implosions," Phys. Rev. Lett. **124**, 145001 (2020).

[31]K. L. Baker, S. MacLaren, O. Jones, B. K. Spears, P. K. Patel, R. Nora, L. Divol, O. L. Landen, G. J. Anderson, J. Gaffney, M. Kruse, O. A. Hurricane, D. A. Callahan, A. R. Christopherson, J. Salmonson, E. P. Hartouni, T. Döppner, E. Dewald, R. Tommasini, C. A. Thomas, C. Weber, D. Clark, D. T. Casey, M. Hohenberger, S. Khan, T. Woods, J. L. Milovich, R. L. Berger, D. Strozzi, A. Kritcher, B. Bachmann, R. Benedetti, R. Bionta, P. M. Celliers, D. Fittinghoff, R. Hatarik, N. Izumi, M. G. Johnson, G. Kyrala, T. Ma, K. Meaney, M. Millot, S. R. Nagel, A. Pak, P. L. Volegov, C. Yeamans, and C. Wilde, "Alpha heating of indirect drive layered implosions on the National Ignition Facility," Phys. Rev. Lett. (submitted) (2021).

[32]A. B. Zylstra, O. A. Hurricane, D. A. Callahan, A. L. Kritcher, J. Ralph, H. F. Robey, J. S. Ross, C. Young, K. Baker, D. Casey, T. Döppner, L. Divol, M. Hohenberger, S. L. Pape, A. Pak, P. Patel, R. Tommasini, S. Ali, B. Bachmann, R. Benedetti, D. Berger, R. Betti, S. Bhandarkar, R. Bionta, N. Birge, E. Bond, D. Bradley, T. Braun, T. Briggs, M. Bruhn, H. Chen, P. Celliers, T. Chapman, C. Choate, A. Christopherson, D. Clark, E. Dewald, J.-M. D. Nicola, T. Dittrich, M. J. Edwards, M. Farrell, J. Field, D. Fittinghoff, J. Frenje, J. Gaffney, G. Grim, S. Haan, K. Hahn, G. Hall, J. Hammer, E. Hartouni, J. Heebner, V. Hernandez, H. Herrmann, M. Herrmann, D. Hinkel, J. Holder, L. B. Hopkins, W. Hsing, K. Humbird, N. Izumi, J. Jeet, M. Gatu Johnson, O. Jones, S. Kerr, S. Khan, J. Kilkenny, Y. Kim, H. Geppert Kleinrath, V. Geppert Kleinrath, J. Kline, J. Kroll, C. Kong, O. L. Landen, D. Larson, N. C. Lemos, J. Lindl, A. Mackinnon, B. MacGowan, S. Maclaren, A. MacPhee, D. Mariscal, E. Marley, L. Masse, K. Meaney, N. Meezan, P. Michel, M. Millot, J. Milovich, J. Moody, A. Moore, K. Newman, A. Nikroo, R. Nora, L. Pelz, L. Peterson, N. Rice, H. Rinderknecht, M. Rosen, M. Rubery, J. Salmonson, J. Sater, D. Schlossberg, M. Schneider, K. Sequoia, S. Shin, V. Smalyuk, B. Spears, P. Springer, M. Stadermann, S. Stoupin, D. Strozzi, C. Thomas, E. Tubman, R. Town, C. Weber, K. Widmann, C. Wilde, T. Woods, B. Woodworth, B. Van Wonterghem, P. Volegov, and S. Yang, "Burning plasma achieved in inertial fusion," Nature **601**, 542–548 (2022).

[33]A. L. Kritcher, C. Young, H. F. Robey, C. Weber, A. B. Zylstra, O. A. Hurricane, D. A. Callahan, J. Ralph, J. S. Ross, K. Baker, D. Casey, T. Döppner, L. Divol, M. Hohenberger, S. L. Pape, A. Pak, P. Patel, R. Tommasini, S. Ali, B. Bachmann, R. Benedetti, D. Berger, R. Betti, S. Bhandarkar, R. Bionta, N. Birge, E. Bond, D. Bradley, T. Braun, T. Briggs, M. Bruhn, H. Chen, P. Celliers, T. Chapman, C. Choate, A. Christopherson, D. Clark, E. Dewald, J.-M. D. Nicola, T. Dittrich, M. J. Edwards, M. Farrell, J. Field, D. Fittinghoff, J. Frenje, J. Gaffney, G. Grim, S. Haan, K. Hahn, G. Hall, J. Hammer, E. Hartouni, J. Heebner, V. Hernandez, H. Herrmann, M. Herrmann, D. Hinkel, J. Holder, L. B. Hopkins, W. Hsing, K. Humbird, N. Izumi, J. Jeet, M. Gatu Johnson, O. Jones, S. Kerr, S. Khan, J. Kilkenny, Y. Kim, H. Geppert Kleinrath, V. Geppert Kleinrath, J. Kline, J. Kroll, C. Kong, O. L. Landen, D. Larson, N. C. Lemos, J. Lindl, A. Mackinnon, B. MacGowan, S. Maclaren, A. MacPhee, D. Mariscal, E. Marley, L. Masse, K. Meaney, N. Meezan, P. Michel, M. Millot, J. Milovich, J. Moody, A. Moore, K. Newman, A. Nikroo, R. Nora, L. Pelz, L. Peterson, N. Rice, H. Rinderknecht, M. Rosen, M. Rubery, J. Salmonson, J. Sater, D. Schlossberg, M. Schneider, K. Sequoia, S. Shin, V. Smalyuk, B. Spears, P. Springer, M. Stadermann, S. Stoupin, D. Strozzi, C. Thomas, E. Tubman, R. Town, K. Widmann, C. Wilde, T. Woods, B. Woodworth, B. Van Wonterghem, P. Volegov, M. Yamaguchi, and S. Yang, "Design of implosions reaching the burning plasma regime," Nat. Phys. **18**, 251–258 (2022).

[34]J. S. Ross, J. Ralph, A. B. Zylstra, A. L. Kritcher, H. F. Robey, C. Young, O. A. Hurricane, D. A. Callahan, K. Baker, D. Casey, T. Döppner, L. Divol, M. Hohenberger, S. L. Pape, A. Pak, P. Patel, R. Tommasini, S. Ali, B. Bachmann, R. Benedetti, D. Berger, R. Betti, S. Bhandarkar, R. Bionta, N. Birge, E. Bond, D. Bradley, T. Braun, T. Briggs, M. Bruhn, H. Chen, P. Celliers, T. Chapman, C. Choate, A. Christopherson, D. Clark, E. Dewald, J.-M. D. Nicola, T. Dittrich, M. J. Edwards, M. Farrell, J. Field, D. Fittinghoff, J. Frenje, J. Gaffney, G. Grim, S. Haan, K. Hahn, G. Hall, J. Hammer, E. Hartouni, J. Heebner, V. Hernandez, H. Herrmann, M. Herrmann, D. Hinkel, J. Holder, L. B. Hopkins, W. Hsing, K. Humbird, N. Izumi, J. Jeet, M. Gatu Johnson, O. Jones, S. Kerr, S. Khan, J. Kilkenny, Y. Kim, H. Geppert Kleinrath, V. Geppert Kleinrath, J. Kline, J. Kroll, C. Kong, O. L. Landen, D. Larson, N. C. Lemos, J. Lindl, A. Mackinnon, B. MacGowan, S. Maclaren, A. MacPhee, D. Mariscal, E. Marley, L. Masse, K. Meaney, N. Meezan, P. Michel, M. Millot, J. Milovich, J. Moody, A. Moore, K. Newman, A. Nikroo, R. Nora, L. Pelz, L. Peterson, N. Rice, H. Rinderknecht, M. Rosen, M. Rubery, J. Salmonson, J. Sater, D. Schlossberg, M. Schneider, K. Sequoia, S. Shin, V. Smalyuk, B. Spears, P. Springer, M. Stadermann, S. Stoupin, D. Strozzi, C. Thomas, E. Tubman, R. Town, C. Weber, K. Widmann, C. Wilde, T. Woods, B. Woodworth, B. Van Wonterghem, P. Volegov, M. Yamaguchi, and S. Yang, "Achieving a burning plasma state in inertial confinement fusion implosions: Experimental analysis," Nature (submitted) (2021).

[35]S. Le Pape, L. F. Berzak Hopkins, L. Divol, A. Pak, E. L. Dewald, S. Bhandarkar, L. R. Bennedetti, T. Bunn, J. Biener, J. Crippen, D. Casey, D. Edgell, D. N. Fittinghoff, M. Gatu-Johnson, C. Goyon, S. Haan, R. Hatarik, M. Havre, D. D.-M. Ho, N. Izumi, J. Jaquez, S. F. Khan, G. A. Kyrala, T. Ma, A. J. Mackinnon, A. G. MacPhee, B. J. MacGowan, N. B. Meezan, J. Milovich, M. Millot, P. Michel, S. R. Nagel, A. Nikroo, P. Patel, J. Ralph, J. S. Ross, N. G. Rice, D. Strozzi, M. Stadermann, P. Volegov, C. Yeamans, C. Weber, C. Wild, D. Callahan, and O. A. Hurricane, "Fusion Energy output greater than the kinetic energy of an imploding shell at the National Ignition Facility," Phys. Rev. Lett. **120**, 245003 (2018).

[36]K. L. Baker, O. Jones, D. Clark, P. K. Patel, C. A. Thomas, S. MacLaren, T. Doppner, E. Dewald, R. Tomassini, B. K. Spears, J. Salmonson, C. Weber, D. T. Casey, M. Hohenberger, S. Khan, O. L. Landen, O. A. Hurricane, D. A. Callahan, R. Nora, T. Woods, J. L. Milovich, R. L. Berger, D. Strozzi, A. Kritcher, B. Bachmann, R. Benedetti, R. Bionta, P. M. Celliers, D. Fittinghoff, C. Goyon, R. Hatarik, N. Izumi, M. Gatu Johnson, G. Kyrala, T. Ma, K. Meaney, M. Millot, S. R. Nagel, D. Turnbull, P. L. Volegov, C. Yeamans, C. Wilde, P. Amendt, and V. Smalyuk, "Hydroscaling high adiabat layered implosions," Bull. Am. Phys. Soc. **65**, 176 (2020).

[37]P. Amendt, D. Ho, Y. Ping, V. Smalyuk, S. Khan, J. Lindl, D. Strozzi, R. Tommasini, M. Belyaev, C. Cerjan, O. Jones, W. Kruer, N. Meezan, H. Robey, F. Tsung, C. Weber, and C. Young, "Ultra-high (>30%) coupling efficiency designs for demonstrating central hot-spot ignition on the National Ignition Facility using a Frustraum," Phys. Plasmas **26**, 082707 (2019).

[38]H. F. Robey, L. Berzak Hopkins, J. L. Milovich, and N. B. Meezan, "The I-Raum: A new shaped *Hohlraum* for improved inner beam propagation in indirectly-driven ICF implosions on the National Ignition Facility," Phys. Plasmas **25**, 012711 (2018).

[39]D. A. Callahan, O. A. Hurricane, J. E. Ralph, C. A. Thomas, K. L. Baker, L. R. Benedetti, L. F. Berzak Hopkins, D. T. Casey, T. Chapman, C. E. Czajka, E. L. Dewald, L. Divol, T. Döppner, D. E. Hinkel, M. Hohenberger, L. C. Jarrott, S. F. Khan, A. L. Kritcher, O. L. Landen, S. L. Pape, S. A. MacLaren, L. P. Masse, N. B. Meezan, A. E. Pak, J. D. Salmonson, D. T. Woods, N. Izumi, T. Ma, D. A. Mariscal, S. R. Nagel, J. L. Kline, G. A. Kyrala, E. N. Loomis, A. Yi, A. B. Zylstra, and S. H. Batha, "Exploring the limits of case-to-capsule ratio, pulse length, and picket energy for symmetric *Hohlraum* drive on the National Ignition Facility Laser," Phys. Plasmas **25**, 056305 (2018).

[40]N. Izumi, D. T. Woods, N. B. Meezan, J. D. Moody, O. L. Landen, L. Divol, H. Chen, D. A. Callahan, M. Hohenberger, A. L. Kritcher, D. T. Casey, M. D. Rosen, J. S. Ross, M. B. Schneider, M. J. Edwards, and W. W. Hsing, "Low mode implosion symmetry sensitivity in low gas-fill NIF cylindrical *Hohlraums*," Phys. Plasmas **28**, 022706 (2021).

[41]O. L. Landen, J. D. Lindl, S. W. Haan, D. T. Casey, P. M. Celliers, D. N. Fittinghoff, N. Gharibyan, V. N. Goncharov, G. P. Grim, E. P. Hartouni, O. A. Hurricane, B. J. MacGowan, S. A. MacLaren, K. D. Meaney, M. Millot, J. L. Milovich, P. K. Patel, H. S. Robey, P. T. Springer, P. L. Volegov, and M. J. Edwards, "Fuel convergence sensitivity in indirect drive implosions," Phys. Plasmas **28**, 042705 (2021).

[42]A. J. MacKinnon, N. B. Meezan, J. S. Ross, S. L. Pape, L. Berzak Hopkins, L. Divol, D. Ho, J. Milovich, A. Pak, J. Ralph, T. Döppner, P. K. Patel, C. Thomas, R. Tommasini, S. Haan, A. G. MacPhee, J. McNaney, J. Caggiano, R. Hatarik, R. Bionta, T. Ma, B. Spears, J. R. Rygg, L. R. Benedetti, R. P. J. Town, D. K. Bradley, E. L. Dewald, D. Fittinghoff, O. S. Jones, H. R. Robey, J. D. Moody, S. Khan, D. A. Callahan, A. Hamza, J. Biener, P. M. Celliers, D. G. Braun, D. J. Erskine, S. T. Prisbrey, R. J. Wallace, B. Kozioziemski, R. Dylla-Spears, J. Sater, G. Collins, E. Storm, W. Hsing, O. Landen, J. L. Atherton, J. D. Lindl, M. J. Edwards, J. A. Frenje, M. Gatu-Johnson, C. K. Li, R. Petrasso, H. Rinderknecht, M. Rosenberg, F. H. Séguin, A. Zylstra, J. P. Knauer, G. Grim, N. Guler, F. Merrill, R. Olson, G. A. Kyrala, J. D. Kilkenny, A. Nikroo, K. Moreno, D. E. Hoover, C. Wild, and E. Werner, "High-density carbon ablator experiments on the National Ignition Facility," Phys. Plasmas **21**, 056318 (2014).

[43]D. D. Ho, "Ignition capsule design with a high-density carbon (HDC) ablator for the National Ignition Facility (NIF)," Bull. Am. Phys. Soc. **52**, 2 (2007).

[44]D. D.-M. Ho, S. W. Haan, J. D. Salmonson, D. S. Clark, J. D. Lindl, J. L. Milovich, C. A. Thomas, L. F. Berzak Hopkins, and N. B. Meezan, "Implosion configurations for robust ignition using high-density carbon (diamond) ablator for indirect-drive ICF at the National Ignition Facility," J. Phys. Conf. Ser. **717**, 012023 (2016).

[45]D. G. Hicks, T. R. Boehly, P. M. Celliers, D. K. Bradley, J. H. Eggert, R. S. McWilliams, R. Jeanloz, and G. W. Collins, "High-precision measurements of the diamond Hugoniot in and above the melt region," Phys. Rev. B **78**, 174102 (2008).

[46]D. S. Clark, A. L. Kritcher, S. A. Yi, A. B. Zylstra, S. W. Haan, and C. R. Weber, "Capsule physics comparison of National Ignition Facility implosion designs using plastic, high density carbon, and beryllium ablators," Phys. Plasmas **25**, 032703 (2018).

[47]J. D. Lindl, P. Amendt, R. L. Berger, S. G. Glendinning, S. H. Glenzer, S. W. Haan, R. L. Kauffman, O. L. Landen, and L. J. Suter, "The physics basis for ignition using indirect-drive targets on the National Ignition Facility," Phys. Plasmas **11**, 339 (2004).

[48]D. H. Cohen, O. L. Landen, and J. J. MacFarlane, "Numerical modeling of *Hohlraum* radiation conditions: Spatial and spectral variations due to sample position, beam pointing, and *Hohlraum* geometry," Phys. Plasmas **12**, 122703 (2005).